

Supporting Information for
**Identifying the Imperative Role of Metal-Olefin Interactions in Catalytic C–O
Reductive Elimination from Nickel(II)**

Trevor D. Lohrey,^a Alexander Q. Cusumano,^a William A. Goddard III,^{b,} and Brian M. Stoltz^{a,*}*

^a *Warren and Katharine Schlinger Laboratory of Chemistry and Chemical Engineering, Division
of Chemistry and Chemical Engineering, California Institute of Technology, MC 101-20,
Pasadena, California 91125, United States*

^b *Materials and Process Simulation Center, Beckman Institute, California Institute of
Technology, Pasadena, California 91125, United States*

stoltz@caltech.edu

wag@caltech.edu

Table of Contents:

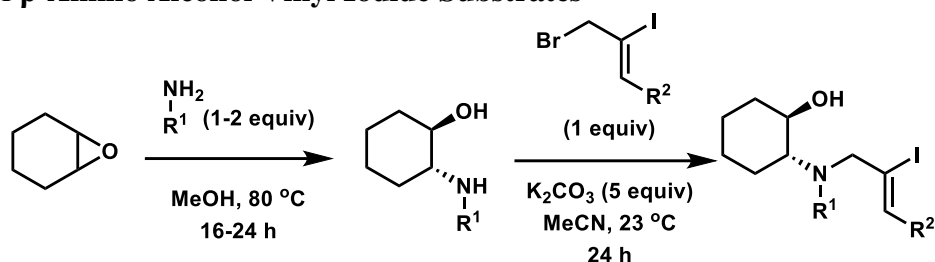
Materials and Methods	S2
List of Abbreviations	S2
Synthesis of β -Amino Alcohol Vinyl Iodide Substrates	S3
Synthesis of Aryl Iodide Substrate	S5
General Procedure for Nickel-Catalyzed Cycloetherification	S6
Synthetic Procedures and Characterization Data for Isolated Nickel Compounds	S8
Proposed Mechanisms of Formation for 4 , 5 , and 7	S14
X-Ray Crystallographic Procedures, Refinement Details, and Additional Figures	S16
Computational Methodologies.....	S21
NMR Spectra of New Compounds and Key Experiments.....	S43
References	S66

Materials and Methods

Unless otherwise stated, catalytic and synthetic organometallic reactions were performed in a nitrogen glovebox using dry, deoxygenated solvents. Solvents were dried by passage through an activated alumina column under argon. Organic reagents were purchased from Sigma-Aldrich, Acros Organics, Strem, Oakwood Chemical, or Alfa Aesar and used as received unless otherwise stated. Ni(COD)₂ was purchased from Strem and used as received, or recrystallized at -40 °C from a 1:5 toluene/Et₂O mixture prior to use. Reaction progress was monitored by thin-layer chromatography (TLC) or Agilent 1290 UHPLC-MS. TLC was performed using E. Merck silica gel 60 F254 precoated glass plates (0.25 mm) and visualized by UV fluorescence quenching or KMnO₄ staining. Silicycle SiliaFlash® P60 Academic Silica gel (particle size 40–63 μm) was used for flash column chromatography. ¹H NMR spectra were recorded on a Bruker 400 MHz spectrometer and are reported relative to residual CHCl₃ (δ 7.26 ppm) or CHD₅ (δ 7.16 ppm). ¹³C NMR spectra were recorded on a Bruker 400 MHz spectrometer (100 MHz) and are reported relative to CDCl₃ (δ 77.16 ppm) or C₆D₆ (δ 128.06 ppm). ³¹P NMR spectra were recorded on a Bruker 400 MHz spectrometer (162 MHz) and are reported relative to a free PCy₃ internal standard. Data for ¹H NMR are reported as follows: chemical shift (δ ppm) (multiplicity, coupling constant (Hz), integration). Multiplicities are reported as follows: s = singlet, d = doublet, t = triplet, q = quartet, p = pentet, sept = septuplet, m = multiplet. Data from ¹³C and ³¹P NMR spectra are reported in terms of chemical shifts (δ ppm). IR spectra were obtained by use of a Perkin Elmer Spectrum BXII spectrometer using thin films deposited on NaCl plates and reported in frequency of absorption (cm⁻¹). High resolution mass spectra (HRMS) of new organics were obtained from the Caltech Mass Spectral Facility.

List of Abbreviations:

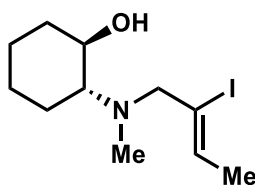
TLC – thin-layer chromatography, COD – 1,5-cyclooctadiene, Et₂O – diethyl ether

Synthesis of β -Amino Alcohol Vinyl Iodide Substrates

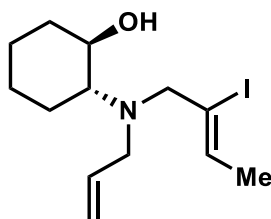
New vinyl iodide substrates (**1a**, **1d**) were synthesized by a two-pot procedure akin to that described in our previous report.¹ A solution of cyclohexene oxide (1.0 equiv) and primary amine (1-2 equiv) in methanol ([amine] = 2 M) was heated in a sealed scintillation vial at 80 °C for 16–24 h, after which time the volatile components of the reaction mixture were removed by rotary evaporation to yield the desired β -amino alcohols, which were used in the following step without further purification.

To a solution of β -amino alcohol (1 equiv) dissolved in MeCN (5-8 mL) was added K_2CO_3 (5 equiv) followed by the appropriate allylic bromide (1 equiv). The resulting mixture was stirred at ambient temperature (ca. 23 °C) for 24 h. The reaction mixture was then filtered through Celite and concentrated by rotary evaporation. The resulting crude residues were purified by silica gel chromatography using hexanes/EtOAc as a mobile phase to yield β -amino alcohol vinyl iodides (**1a**, **1d**).

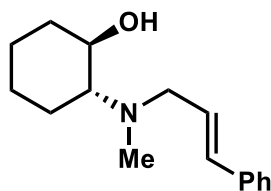
Compound **3** was synthesized by this same procedure, employing cinnamyl bromide in the second step in place of an iodinated allylic bromide.



Compound **1a**: Isolated as a colorless oil from a 2 mmol scale reaction. Yield: 115 mg, 19%. ¹H NMR (400 MHz, 298 K, CDCl₃): δ = 5.83 (q, J = 6.0 Hz, 1H), 4.02 (s, 1H), 3.41 (td, J = 4.7, 9.8 Hz, 1H), 3.27 (d, J = 13.4 Hz, 1H), 3.08 (d, J = 13.4 Hz, 1H), 2.15 (s, 3H), 2.12 (td, J = 1.9, 5.4 Hz, 1H), 1.80 (d, J = Hz, 3H), 1.78-1.62 (m, 4H), 1.33-1.08 (m, 4H). ¹³C NMR (100 MHz, 298 K, CDCl₃): δ = 132.2, 111.8, 69.5, 69.0, 65.3, 35.7, 33.4, 25.6, 24.3, 22.7, 21.9. FT-IR (neat film/NaCl): 3474, 2929, 2854, 1763, 1450, 1304, 1206, 1167, 1081, 1032 cm⁻¹. HRMS (MM: TOF-MS ES⁺): m/z calc'd for C₁₁H₂₁NOI, [M+H]⁺ = 310.0668; found = 310.0662.

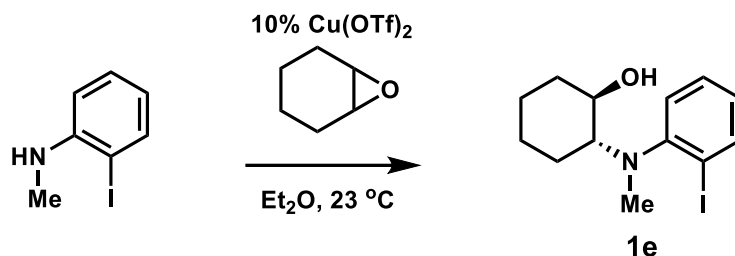


Compound **1d**: Isolated as a yellow oil from a 1 mmol scale reaction. Yield: 50 mg, 15%. ^1H NMR (400 MHz, 298 K, CDCl_3): δ = 5.92-5.78 (m, 2H), 5.14 (d, J = 26.2 Hz, 1H), 5.13 (s, 1H), 3.90 (s, 1H), 3.48-3.36 (m, 2H), 3.26 (dt, J = Hz, 1H), 3.02 (d, J = 13.8 Hz, 1H), 2.91 (dd, J = 7.4, 14.0 Hz, 1H), 2.44-2.34 (m, 1H), 2.17-2.08 (m, 1H), 1.80 (dd, J = 2.6, 6.3 Hz, 3H), 1.78-1.66 (m, 3H), 1.32-1.00 (m, 4H). ^{13}C NMR (100 MHz, 298 K, CDCl_3): δ = 136.8, 132.8, 117.6, 111.8, 69.1, 64.7, 60.7, 52.2, 33.3, 25.7, 24.3, 23.4, 22.0. FT-IR (neat film/ NaCl): 3485, 2932, 2857, 2358, 1447, 1300, 1206, 1080, 991, 917 cm^{-1} . HRMS (MM: TOF-MS ESI $^+$): m/z calc'd for $\text{C}_{13}\text{H}_{23}\text{NOI}$, $[\text{M}+\text{H}]^+ = 336.0824$; found = 336.0813.

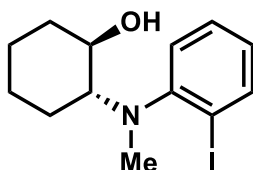


Compound **3**: Isolated as a pale yellow semi-crystalline solid from a 1 mmol scale reaction. Yield: 165 mg, 67%. ^1H NMR (400 MHz, 298 K, C_6D_6): δ = 7.28-7.23 (m, 2H), 7.16-7.11 (m, 2H), 7.09-7.04 (m, 1H), 6.38 (d, J = 15.9 Hz, 1H), 6.07 (ddd, J = 6.3, 6.9, 15.9 Hz, 1H), 3.36 (td, J = 4.5, 10.4 Hz, 1H), 3.08 (ddd, J = 1.4, 6.2, 13.7 Hz, 1H), 2.83 (ddd, J = 1.1, 7.0, 13.7 Hz, 1H), 2.29-2.21 (m, 2H), 2.00 (s, 3H), 1.55-1.43 (m, 3H), 1.42-1.30 (m, 1H), 1.08-0.92 (m, 2H), 0.91-0.79 (m, 1H). ^{13}C NMR (100 MHz, 298 K, C_6D_6): δ = 137.8, 132.6, 129.2, 129.1, 127.1, 69.8, 69.8, 56.9, 36.8, 34.4, 26.1, 24.8, 22.2. FT-IR (neat film/ NaCl): 3447, 2931, 2857, 1450, 1079, 1030, 965, 743, 693 cm^{-1} . HRMS (MM: TOF-MS ESI $^+$): m/z calc'd for $\text{C}_{16}\text{H}_{24}\text{NO}$, $[\text{M}+\text{H}]^+ = 246.1858$; found = 246.1854.

Synthesis of Aryl Iodide Substrate

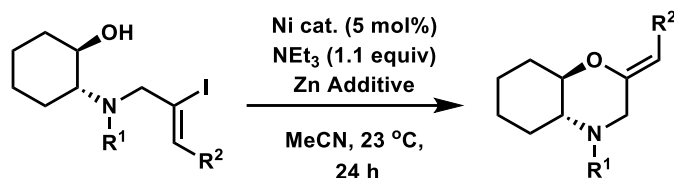


In an adaptation of a reported procedure,² cyclohexene oxide (197 mg, 2.01 mmol, 1.0 equiv) and *N*-methyl-2-iodoaniline (469 mg, 2.01 mmol, 1.0 equiv) were dissolved in dry Et_2O (10 mL). $\text{Cu}(\text{OTf})_2$ (72 mg, 0.20 mmol, 0.1 equiv) was then added, and the reaction mixture was stirred at ca. $23\text{ }^\circ\text{C}$ overnight. The reaction mixture was then filtered through Celite and concentrated by rotary evaporation. Following purification by silica gel chromatography with a hexanes/ EtOAc mobile phase, compound **1e** was isolated as a colorless oil (189 mg, 29%).



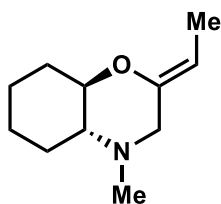
Compound **1e**: ^1H NMR (400 MHz, 298 K, CDCl_3): δ = 7.85 (dd, J = 1.4, 7.9 Hz, 1H), 7.34-7.27 (m, 1H), 7.21 (dd, J = 1.2, 7.9 Hz, 1H), 6.82 (td, J = 1.5, 7.3 Hz, 1H), 3.83 (s, 1H), 3.65 (td, J = 4.2, 9.9 Hz, 1H), 2.89 (ddd, J = 3.4, 9.9, 11.7 Hz, 1H), 2.69 (s, 3H), 2.21-2.12 (m, 1H), 1.87-1.79 (m, 1H), 1.79-1.68 (m, 2H), 1.59-1.46 (m, 1H), 1.40-1.13 (m, 3H). ^{13}C NMR (100 MHz, 298 K, CDCl_3): δ = 153.4, 140.3, 129.2, 126.3, 125.2, 99.9, 70.7, 68.2, 34.6, 33.8, 25.5, 24.5, 24.5. FT-IR (neat film/ NaCl): 3486, 2933, 2858, 1578, 1468, 1285, 1076, 1045, 1013, 984, 754 cm^{-1} . HRMS (MM: TOF-MS ESI⁺): m/z calc'd for $\text{C}_{13}\text{H}_{19}\text{NOI}$, $[\text{M}+\text{H}]^+$ = 332.0511; found = 332.0516.

General Procedure for Nickel-Catalyzed Cycloetherification

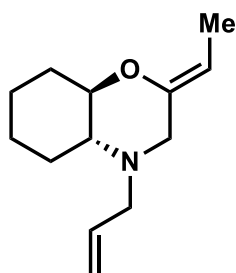


In an N₂-filled glovebox, to a vial containing vinyl iodide substrate (0.135 mmol) was added MeCN (0.9 mL, 0.15 M) and triethylamine (21 μ L, 1.1 equiv). Once a homogeneous solution was obtained by gentle stirring, it was then added by pipette to a 1 dram vial containing Ni precatalyst (e.g. 1.8 mg/5 mol% of Ni(COD)₂) and a zinc additive (if applicable, e.g. 17.7 mg/2 equiv of Zn dust, or 12.3 mg/0.25 equiv of Zn(OTf)₂). The reaction mixture was then stirred in the glovebox at ca. 23 °C for 24 h (unless specified otherwise). The reaction mixture was then removed from the glovebox, exposed to ambient atmosphere, filtered through Celite, and concentrated by rotary evaporation. Enol ether products and unreacted starting material were then isolated by silica gel chromatography, using hexanes/EtOAc as a mobile phase. In all cases, the R_f values of the enol ether products were found to be significantly lower than those of the vinyl iodide starting materials.

Note that reactions conducted with other Ni precatalysts (e.g. **5**, **6**, **7**) were carried out such that the total Ni content of the reaction equaled 5 mol%. Additionally, reactions conducted in solvents other than MeCN used the same quantity of solvent (0.9 mL) to maintain an identical starting concentration.

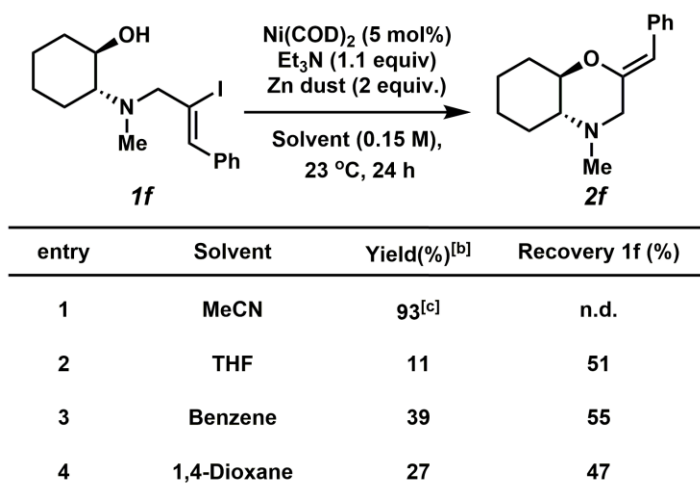


Compound **2a**: Isolated as a yellow oil from a 0.135 mmol scale reaction. Reaction time: 24 h. Yield: 13.1 mg, 54%. ¹H NMR (400 MHz, 298 K, CDCl₃): δ = 4.65 (qd, J = 1.5, 6.7 Hz, 1H), 3.32 (qd, J = 4.3, 9.2 Hz, 1H), 3.16 (d, J = 12.3 Hz, 1H), 2.81 (d, J = 11.6 Hz, 1H), 2.26 (s, 3H), 2.12-1.99 (m, 2H), 1.91-1.82 (m, 1H) 1.58 (dd, J = 2.0, 7.7 Hz, 3H), 1.50-1.38 (m, 1H), 1.37-1.20 (m, 4H), 1.18-1.05 (m, 1H). ¹³C NMR (100 MHz, 298 K, CDCl₃): δ = 148.4, 103.8, 80.6, 67.5, 58.7, 41.5, 31.4, 28.0, 24.8, 24.4, 9.63. FT-IR (neat film/NaCl): 2926, 2861, 1680, 1454, 1361, 1330, 1070, 1026 cm⁻¹. HRMS (MM: TOF-MS ESI⁺): m/z calc'd for C₁₁H₂₀NO, [M+H]⁺ = 182.1545; found = 182.1539.



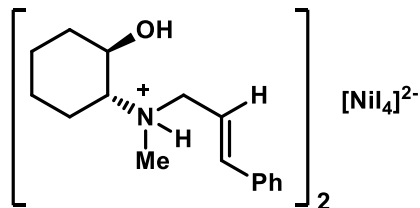
Compound **2d**: Isolated as a red-brown oil from a 0.135 mmol scale reaction. Reaction time: 44h. Yield: 11.4 mg, 41%. 50% of the starting material was also recovered. ^1H NMR (400 MHz, 298 K, CDCl_3): δ = 5.86 (qdd, J = 5.4, 8.1, 16.0 Hz, 1H), 5.21 (m, 1H), 5.17 (s, 1H), 4.61 (qd, J = 1.3, 6.7 Hz, 1H), 3.49 (dd, J = 5.4, 13.6 Hz, 1H), 3.35 (qd, J = 4.3, 9.0 Hz, 1H), 3.24 (d, J = 12.5 Hz, 1H), 2.85-2.75 (m, 2H), 2.17-1.98 (m, 3H), 1.81-1.69 (m, 2H), 1.57 (dd, J = 1.9, 6.7 Hz, 3H), 1.50-1.38 (m, 1H), 1.37-1.19 (m, 3H), 1.18-1.07 (m, 1H). ^{13}C NMR (100 MHz, 298 K, CDCl_3): δ = 148.7, 134.2, 118.9, 103.3, 80.5, 65.3, 55.9, 54.8, 31.6, 28.1, 24.8, 24.4, 9.63. FT-IR (neat film/ NaCl): 2937, 2864, 1734, 1678, 1451, 1418, 1330, 1202, 1070, 918 cm^{-1} . HRMS (MM: TOF-MS ESI $^+$): m/z calc'd for $\text{C}_{13}\text{H}_{22}\text{NO}$, $[\text{M}+\text{H}]^+ = 208.1701$; found = 208.1692.

Table S1. Results of Ni-catalyzed cycloetherification carried out in various solvents.



[a] Standard conditions: **1f** (0.135 mmol), $\text{Ni}(\text{COD})_2$ (5 mol%), triethylamine (1.1 equiv), Zn dust (2 equiv), Solvent (0.9 mL, 0.15 M). [b] Yield of isolated product. [c] Result taken from reference 1 of the Supporting Information.

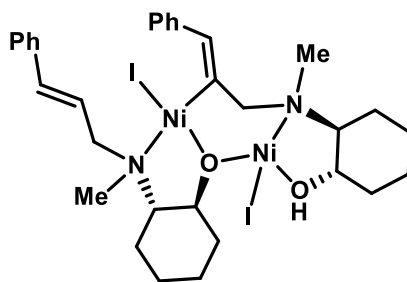
Synthetic Procedures and Characterization Data for Isolated Nickel Compounds



Compound 4

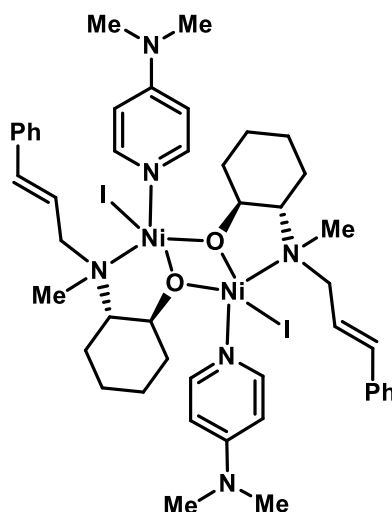
In an N₂-filled glovebox, solid Ni(COD)₂ (37.0 mg, 0.135 mmol) was added to a stirred solution of **1f** (50 mg, 0.135 mmol) in acetonitrile (3 mL). Within several minutes, the colorless solution began to take on an orange hue, followed by the precipitation of black solids and the formation of a silvery mirror on the interior of the reaction vial. After a total reaction time of 15 minutes all of the Ni(COD)₂ had dissolved, at which point the volatile components of the reaction mixture were removed in vacuo. The crude residue was extracted with benzene (1 mL). The orange extracts were filtered through Celite into a clean scintillation vial, and the solution was allowed to stand at ambient temperature for several days. Removal of the mother liquor and brief washes with benzene (2 x 0.5 mL) yielded **4** as pale orange crystals (8.7 mg, 24%). X-ray quality single crystals of **4** were obtained by a repetition of this procedure. m.p.: 176-179 °C. ¹H NMR (400 MHz, C₆D₆, 298K): δ 7.79 (bs), 7.27 (s), 5.54 (bs), 3.57 (bs), 2.91 (bs), 2.24 (bs), 1.84 (bs, overlapped), 1.41 (bs, overlapped), 1.31 (bs, overlapped), 1.23 (bs, overlapped), 0.90 (bm), 0.54 (bs). HRMS (MM: TOF-MS ESI⁻): m/z calc'd for NiI₃, [NiI₄-I]⁻ = 438.6488; found = 438.6488.

Additional anions containing both organic and inorganic fragments were observed in a low resolution ESI⁻ mass spectrum, including [NiI₄C₁₀H₁₄N]⁻ found at m/z = 713.7 (calc'd m/z = 713.6659) and [NiI₃C₁₀H₁₃N]⁻ found at m/z = 586.0 (calc'd m/z = 585.7536). Both of these anionic species are the result of cyclohexene oxide (C₆H₁₀O) loss from the parent ammonium/ammonia molecule. Given the susceptibility of **4** to hydrolysis, HRMS analysis of these anions was unsuccessful. LC-MS analysis of hydrolyzed **4** shows the presence of compound **3**.



Compound 5

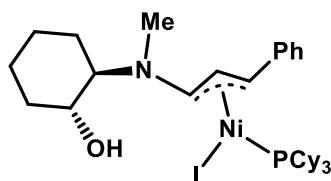
In an N₂-filled glovebox, Ni(COD)₂ (74.0 mg, 0.270 mmol) in Et₂O (3 mL) was added to a stirred solution of **1f** (100 mg, 0.270 mmol) in Et₂O (5 mL). Within seconds, the solution began to take on an orange hue, and within several minutes, a pale orange precipitate began to form. Fine precipitate continued to form over the course of the reaction. After a reaction time of 45 minutes, the stir bar was removed and the reaction mixture was diluted with hexane, leading to the formation of additional precipitate. After storage of the resulting mixture overnight at -40 °C, the mother liquor was removed by pipette, and the isolated solids were washed vigorously with hexane (3 x 5 mL). Following the removal of residual volatile in vacuo, **5** was isolated as a fine orange powder. X-ray quality single crystals of **5-THF** were grown from a THF/hexane solution stored at -40 °C. Yield: 104 mg, 82%. m.p.: decomp. without melting above ca. 160 °C. Anal. Calcd. for C₃₂H₄₄N₂O₂I₂Ni₂ (**5**): C, 44.70; H, 5.16; N, 3.26 %. Found: C, 45.08; H, 5.11; N, 3.19 %. Compound **5** displays a complex, paramagnetically-shifted ¹H NMR spectrum that is not amenable to tabulation.



Compound 6

In an N₂-filled glovebox, a solid mixture of compound **5** (25 mg, 0.029 mmol) and DMAP (7.0 mg, 0.058 mmol) was dissolved in benzene (4 mL). Within seconds, bright orange-yellow crystals began to form. The reaction mixture was allowed to stand at ambient temperature overnight. The following day, the accumulated crystals of **6** were isolated by removing the mother liquor and removing residual volatiles in vacuo. Yield: 27.6 mg, 86%. X-ray quality single crystals of **6** were obtained by repeating the reaction on a smaller scale and lower concentration, slowing the rate of crystallization. m.p. 164-170 °C (slow melting with decomp.). ¹H NMR (400 MHz, CD₂Cl₂, 298K): δ 34.61 (bs), 29.96 (bs), 24.81 (bs), 20.23 (bs), 18.67 (bs), 8.94 (bs), 7.98 (s), 7.22 (s), 6.79 (s), 6.54 (s), 6.28 (s), 5.76 (s), 5.54 (s), 3.44 (bm), 1.95 (s, overlapped), 1.82 (s, overlapped), 1.27 (s, overlapped), -1.22 (bs), -1.60 (s). Anal. Calcd. for C₆₄H₈₂N₆O₂I₂Ni₂ (**6** • 3 C₆H₆): C, 57.43; H, 6.17; N, 6.28 %. Found: C, 56.63; H, 6.18; N, 6.24 %.

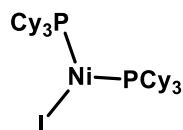
We attribute the low C wt.% found in our elemental combustion analysis to the high benzene content of this highly crystalline compound and its incomplete combustion. The presence of three co-crystallized benzene molecules per molecule of **6** in the solid state is verified in the X-ray crystal structure. Given this consistency, these three benzene molecules were also accounted for in our calculation of the magnetic moment of this compound.



Compound 7

In an N₂-filled glovebox, compound **5** (25 mg, 0.029 mmol) was suspended in Et₂O (4 mL). A solution of tricyclohexylphosphine (16.3 mg, 0.058 mmol) in Et₂O (2 mL) was then added, and the resulting mixture stirred for 20 minutes. The volatile components of the reaction mixture were then removed in vacuo. The crude residue was washed with hexane (3 x 2 mL) and exposed to vacuum to remove residual volatiles. Compound **7** was isolated as pale purple-red solids. Yield: 21.3 mg, 52%. X-ray quality single crystals of **7** were obtained by recrystallizing isolated material from hexane at -40 °C. m.p.: 148-151 °C. ¹H NMR (400 MHz, C₆D₆, 298 K): δ 8.35 (dq, *J* = Hz, 1H), 7.66 (d, *J* = Hz, 2H), 7.23 (t, *J* = Hz, 2H), 7.10 (t, *J* = Hz, 1H), 6.53 (d, *J* = Hz, 1H), 4.34 (ddd, *J* = Hz, 1H), 2.92 (td, *J* = Hz, 1H), 2.72 (s, 3H), 2.71-2.64 (m, 1H), 2.37-2.21 (m, 8H), 2.20-2.01 (m, 12H), 1.96-1.84 (m, 5H), 1.84-1.61 (m, 16H), 1.41-1.16 (m, 23H), 1.03-0.94 (m, 2H), 0.91-0.82 (m, 2H), 0.78-0.58 (m, 2H). ¹³C NMR (100 MHz, C₆D₆, 298 K): δ 137.4, 134.2, 129.0, 127.5, 127.0, 76.3 (d, *J* = 5.7 Hz), 70.2, 59.6, 39.6, 37.3, 34.6, 34.5 (d, *J* = 20.8 Hz), 30.6 (d, *J* = 12.7 Hz), 29.7, 28.2 (d, *J* = 5.0 Hz), 28.1 (d, *J* = 4.9 Hz), 28.1 (d, *J* = 8.3 Hz), 27.0, 25.6, 24.8, 22.7. ³¹P NMR (162 MHz, C₆D₆, 298 K): δ 27.3. Anal. Calcd. for C₃₄H₅₅NOPINi (**7**): C, 57.49; H, 7.80; N, 1.97 %. Found: C, 57.26; H, 7.83; N, 1.82 %.

Compound **7** is isolated as a mixture of diastereomers, in approximately a 1.00:0.28 ratio, which readily co-crystallize (as apparent in the X-ray crystal structure). Based on the NMR spectral data, it appears these diastereomers display different behavior in solution: The major diastereomer of compound **7** displays sharp ¹H NMR resonances, while the minor one appears dynamic, leading to broadened NMR peaks. Some ¹H NMR resonances, particularly those associated with the PCy₃ ligand and cyclohexanol group, are broadened and overlapped: we have listed all of the resonances present in this region of the spectrum, as well as their integrations, which were shown to be reproducible between several batches of material, including after recrystallization or repeated washing of isolated material with hexane. In contrast, the ¹³C NMR spectrum of **7** can easily distinguish between the major and minor diastereomers, as the resonances of the major, non-fluxional diastereomer are of significantly greater intensity than those of the fluxional, minor diastereomer.

**(PCy₃)₂NiI**

While a straightforward synthesis of (PCy₃)₂NiI is reported in the literature,³ the following is an account of our isolation of this material using a vinyl iodide as the halide source. In an N₂-filled glovebox, a solid mixture of Ni(COD)₂ (18.5 mg, 0.067 mmol) and tricyclohexylphosphine (37.8 mg, 0.135 mmol) was dissolved in Et₂O (5 mL), forming a clear orange solution. This solution was added to a stirred solution of **1f** (25 mg, 0.067 mmol) in Et₂O (2 mL). After ca. 3 min, the reaction mixture began to become cloudy, and over the course of the reaction time (45 min), additional pale precipitate continued to form. The stir bar was then removed from the reaction vial, and the mixture was stored at -40 °C overnight. The following day, the mother liquor was removed and the isolated solids were washed with hexane (3 x 2 mL). The washed, pale yellow microcrystalline solids (23.7 mg) were then exposed to vacuum to remove residual volatiles. The combined mother liquor and hexane washes were again stored at -40 °C, leading to the formation of a small second crop of product (4.7 mg), which was isolated similarly. Yield: 28.4 mg, 56%. X-ray quality single crystals of (PCy₃)₂NiI were obtained by the slow evaporation of a Et₂O solution of isolated material. ¹H NMR (400 MHz, C₆D₆, 298K): δ 15.50 (bs), 10.04 (bs), 7.54 (bs), 6.74 (bs), 4.15 (bs), 3.30 (bs), 2.97 (bs), 1.93 (bs), 1.67 (bs, overlapped), 1.56 (bs, overlapped), 1.36 (bs, overlapped), 1.08 (bs, overlapped), 0.37 (bs), -1.15 (bs). ³¹P NMR (162 MHz, C₆D₆, 298K): δ 46.8 (bs).

The identity of the isolated product as (PCy₃)₂NiI was established by X-ray crystallography. Given the lack of reported spectroscopic data for this compound, we herein include its ¹H NMR spectrum and ³¹P NMR spectrum. The X-ray crystal structure of this compound was also previously unknown, and a finalized CIF is also included with this report.

[(COD)NiI]₂

The Ni(I) precatalyst [(COD)NiI]₂ was synthesized by an adaptation of a reported procedure.³ In a N₂-filled glovebox, Ni(COD)₂ (25.0 mg, 0.0909 mmol) was dissolved in a mixture of toluene (5 mL) and COD (0.5 mL). Separately, I₂ (11.5 mg, 0.0909 mmol) was dissolved in 1 mL toluene. Both solutions were chilled to -40 °C in the glovebox freezer. The iodine solution was then added dropwise to the Ni(COD)₂ solution with rapid stirring, leading to a change in color of the reaction mixture from light yellow to orange. After stirring for 2 minutes following the addition, the reaction mixture was stored at -40 °C overnight to ensure the reaction proceeded to completion without decomposition of the product. The following day, the volatile components of the reaction mixture (now a dark orange solution with notable precipitate) were removed in vacuo, and the resulting residue was washed with diethyl ether (3 x 2 mL). [(COD)NiI]₂ was isolated as orange-yellow microcrystalline solids following exposure to vacuum to remove residual volatiles. Yield: 21.8 mg, 82 %. X-ray quality single crystals were grown from a solution of isolated product in a toluene/hexane solution with trace COD at -40 °C.

While crystalline [(COD)NiI]₂ is somewhat stable at ambient temperature (similarly to Ni(COD)₂), we advise that great care must be taken when handling [(COD)NiI]₂ in solution. This highly reactive complex will significantly decompose upon dissolution in benzene or toluene at ambient temperature. The decomposition abates somewhat after an initial generation of dark solids, likely due to the stabilizing effect of free COD in solution. We suggest that any manipulations of this complex are carried out with pre-cooled solvents, with a significant quantity of COD added. We posit the instability of [(COD)NiI]₂ (particularly when compared to (PCy₃)₂NiI, which is generally stable in solution at room temperature) is due to the lability of COD, as well as the dimeric structure of this complex, which likely predisposes this compound to facile thermal or photoinitiated disproportionation.

Proposed Mechanisms of Formation for 4, 5, and 7

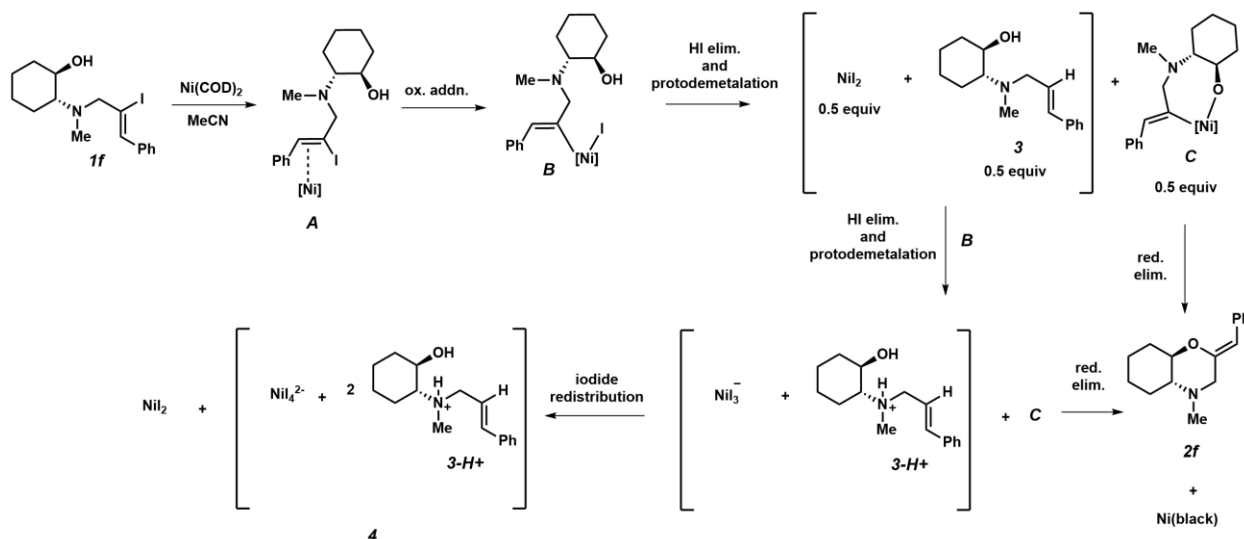


Figure S1. Plausible mechanism for the formation of **3**, **4**, and **2f** from the stoichiometric reaction of $\text{Ni}(\text{COD})_2$ with **1f** in MeCN. [Ni] indicates a solvated Ni center beyond the ligands explicitly drawn. Note that the generation of **2f** is dependent on the formation of **3** via protodemetalation, as the elimination of HI from intermediate **B** (to form **C**) necessitates the presence of a base to deprotonate the free alcohol group. Subsequently, the basic amine group of **3**, in tandem with NiI_2 generated by protodemetalation, may further eliminate HI from additional equivalents of **B**, leading to additional quantities of **2f** as well as the isolated ionic compound **4**.

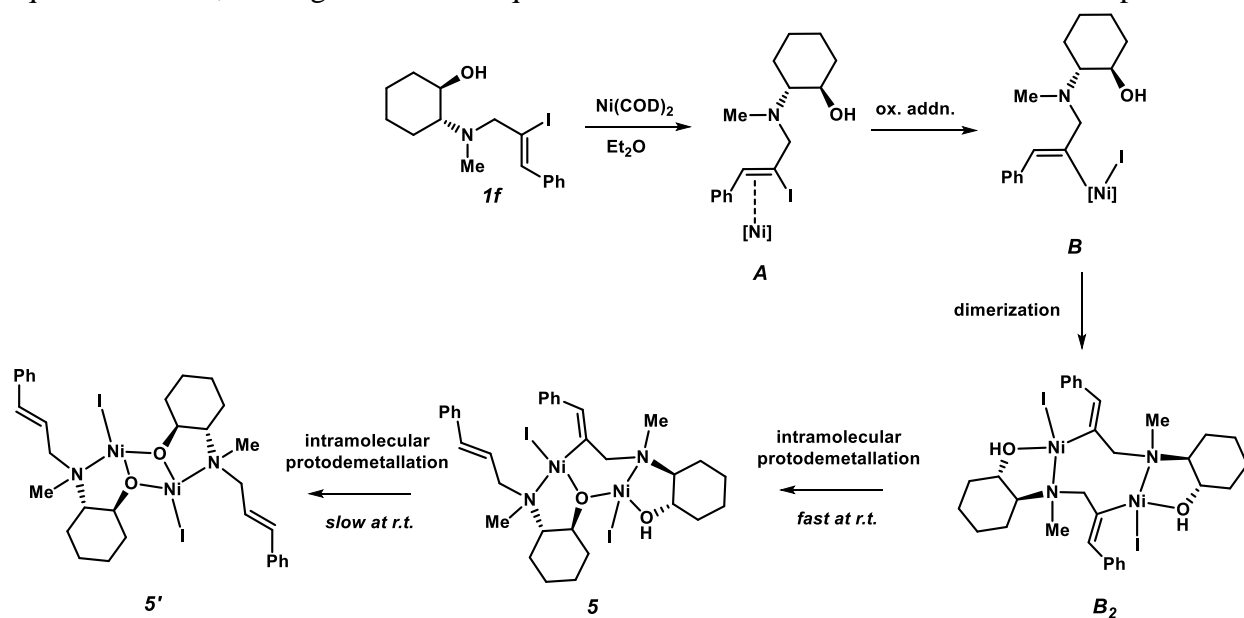


Figure S2. Plausible mechanism for the formation of **5** and **5'** from the stoichiometric reaction of $\text{Ni}(\text{COD})_2$ with **1f** in Et_2O . [Ni] indicates a solvated Ni center beyond the ligands explicitly drawn. The key feature of this reaction is the observation that the poorly coordinating nature of Et_2O leads to the aggregation of Ni(II) species, by virtue of the favorable chelation of the β -

amino cyclohexanol group (as well as the limited thermodynamic favorability of a single equivalent of **1f** chelating to a single Ni center in a tridentate fashion). This dimerization process, which was not observed in MeCN (likely owing to its much greater coordination strength as compared to that of Et₂O), then leads to a rapid internal protodemetalation of one of the Ni-C bonds to generate compound **5**, as isolated. Based on our combined experimental and computational findings, we propose that the slow decomposition of **5** at room temperature involves primarily a second protodemetalation, yielding the dimeric alkoxide-bridged Ni(II) complex **5'** as a major product.

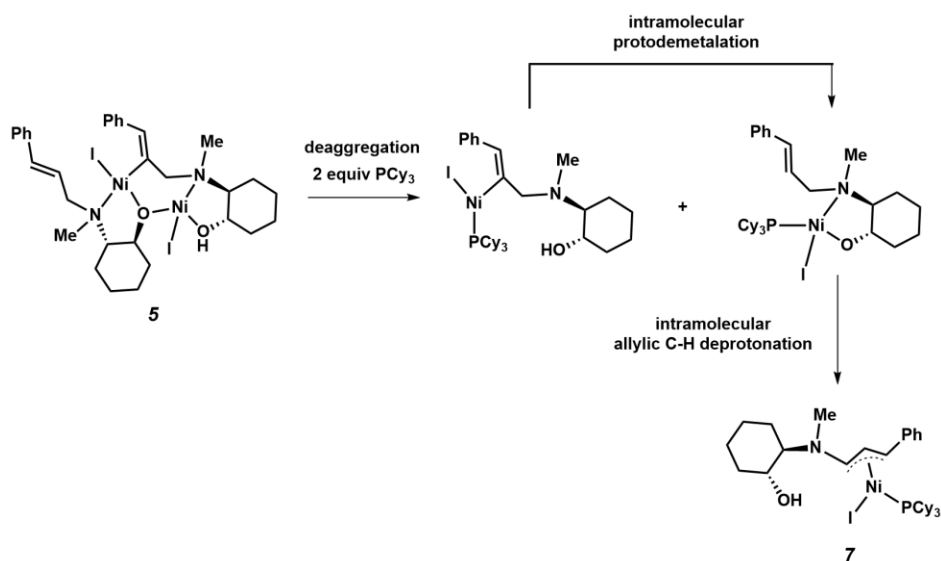


Figure S3. Plausible mechanism for the formation of **7** from the reaction of **5** with PCy₃. Note that the allylic deprotonation likely depends on the formation of mononuclear Ni(II) intermediates, as the structures of compounds **5** and **6** indicate that bridging alkoxide groups are not amenable to promoting this process.

X-Ray Crystallographic Procedures, Refinement Details, and Additional Figures

Single crystal X-ray diffraction data for **4**, **5-THF**, **6**, **7**, [(COD)NiI]₂, and (PCy₃)₂NiI were collected at the Caltech XRCF, using either a Bruker AXS D8 Venture outfitted with a rotating anode Mo-K α ($\lambda = 0.71073 \text{ \AA}$) micro-source, or a Bruker AXS D8 KAPPA with a sealed tube Mo-K α X-ray source. All data collections were conducted at 100 K in a dry nitrogen cryostream. In an N₂-filled glovebox, samples of single crystals were isolated from their mother liquor and coated in a thick hydrocarbon oil for transport to the diffraction facility. In the facility, samples were evaluated by polarized light microscopy, and candidate crystals were mounted on an appropriately-sized MiTiGen MicroLoop for X-ray diffraction analysis. Diffraction data were collected, integrated, and reduced using Bruker AXS APEX3 software, including its associated SAINT and SADABS programs.⁴ Structures were solved and refined using SHELXT and SHELXL-2014,^{5,6} as implemented within WinGX.⁷ The structural model for the allyl complex **7** required modeling of the cyclohexanol moiety over two positions (due to co-crystallization of diastereotopic Ni complexes containing different stereoisomers of the racemic *trans*- β -amino alcohol). The structural model for the asymmetric dinuclear Ni complex **5-THF** required disorder modeling for multiple co-crystallized THF molecules. The PLATON squeeze program⁸ was used to remove electron density associated with a highly disordered Et₂O molecule in the structure of (PCy₃)₂NiI oriented on a 3-fold screw axis (along *c* at $a = b = 1/3$, these void channels are readily observed in a packing diagram of the final model). Thermal ellipsoid plots were generated using Mercury.⁹ Finalized CIFs have been deposited to the Cambridge Crystallographic Data Centre (CCDC), with deposition numbers: 2078291 (**4**), 2078292 (**5-THF**), 2078293 (**6**), 2078294 (**7**), 2078295 ((PCy₃)₂NiI), and 2088878 ([COD)NiI]₂).

Table S2. Crystallographic details and refinement metrics.

	4 • 2(C₆H₆)	5-THF • 3.5(THF)	6 • 3(C₆H₆)	7	[(COD)Ni]₂	(PCy₃)₂NiI Et₂O
Chemical formula	C ₄₄ H ₆₀ I ₄ N ₂ Ni O ₂	C ₅₀ H ₈₀ I ₂ N ₂ Ni ₂ O _{6.5}	C ₆₄ H ₈₂ I ₂ N ₆ Ni ₂ O ₂	C ₃₄ H ₅₅ INNiOP	C ₁₆ H ₂₄ I ₂ Ni ₂	C ₃₆ H ₆₆ INiP ₂
Formula weight	1215.25	1184.38	1338.57	710.37	587.57	746.43
Color, habit	Orange, block	Orange, lath	Orange, block	Purple, block	Orange, needle	Colorless, rod
Temperature (K)	100(2)	100(2)	100(2)	100(2)	100(2)	100(2)
Crystal system	Monoclinic	Triclinic	Orthorhombic	Triclinic	Monoclinic	Rhombohedral
Space group	C2/c	P-1	Pccn	P-1	P2 ₁ /n	R-3c
a (Å)	27.330(11)	12.7775(13)	14.7031(9)	11.0239(9)	7.4617(17)	29.259(3)
b (Å)	9.978(4)	14.7475(15)	17.8228(11)	11.4716(9)	10.686(2)	29.259(3)
c (Å)	17.222(6)	15.2774(16)	23.8035(15)	13.6693(11)	10.939(3)	23.165(2)
α (°)	90	73.188(4)	90	81.983(3)	90	90
β (°)	90.618(13)	86.253(4)	90	78.073(3)	97.511(10)	90
γ (°)	90	70.648(4)	90	75.856(3)	90	120
V (Å ³)	4696(3)	2598.6(5)	6237.7(7)	1632.8(2)	864.8(4)	17175(4)
Z	4	2	4	2	2	18
Density (Mg m ⁻³)	1.719	1.514	1.425	1.455	2.257	1.299
F(000)	2376	1216	2744	740	564	7074
Radiation Type	MoK _α	MoK _α	MoK _α	MoK _α	MoK _α	MoK _α
μ (mm ⁻¹)	3.078	1.961	1.640	1.615	5.735	1.423
Crystal size (mm ³)	0.070 x 0.050 x 0.040	0.200 x 0.100 x 0.030	0.250 x 0.230 x 0.180	0.120 x 0.090 x 0.050	0.100 x 0.020 x 0.015	0.120 x 0.040 x 0.030
Meas. Refl.	28482	110737	48347	44904	13084	85598
Indep. Refl.	4296	9509	5444	6718	1774	3978
R(int)	0.1150	0.0307	0.0399	0.0701	0.0769	0.0742
Completeness to arcsin(0.6*λ)	99.7%	99.5%	98.6%	100.0%	100.0%	99.9%
Final R indices [I > 2σ(I)]	R = 0.0650 R _w = 0.1943	R = 0.0483 R _w = 0.1310	R = 0.0224 R _w = 0.0460	R = 0.0425 R _w = 0.0915	R = 0.0278 R _w = 0.0499	R = 0.0320 R _w = 0.0861
Goodness-of-fit	1.075	1.127	1.080	1.028	1.052	1.067
Δρ _{max} , Δρ _{min} (e Å ⁻³)	4.941, -1.200	1.433, -0.913	0.416, -0.453	0.879, -0.593	0.647, -0.773	1.750, -1.145

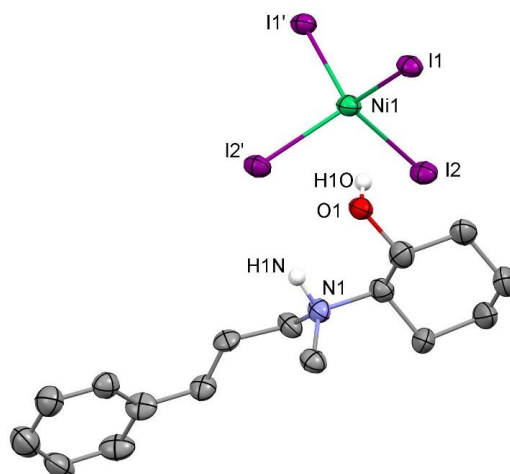


Figure S4. X-ray crystal structure of compound **4** with 50% probability ellipsoids. A co-crystallized benzene molecule and hydrogen atoms (except those on the alcohol and ammonium groups) are excluded for clarity.

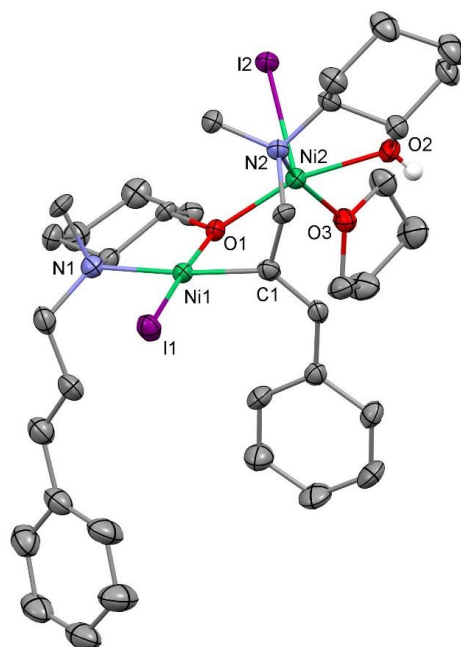


Figure S5. X-ray crystal structure of compound **5-THF** with 50% probability ellipsoids. Co-crystallized THF molecules and hydrogen atoms (except that on the alcohol group) are excluded for clarity. Selected bond distances (Å) and angles (°): Ni1-I1 = 2.4936(9), Ni1-C1 = 1.890(6), Ni1-N1 = 2.043(5), Ni1-O1 = 1.886(4), Ni2-O1 = 1.988(4), Ni2-I2 = 2.6965(9), Ni2-N2 = 2.104(6), Ni2-O2 = 2.073(5), Ni2-O3 = 2.099(4), Ni1-O1-Ni2 = 111.9(2), O1-Ni1-N1 = 86.9(2), O1-Ni-C1 = 87.5(2), C1-Ni1-I1 = 87.65(19), I1-Ni1-N1 = 97.94(15), O2-Ni2-N2 = 80.3(2).

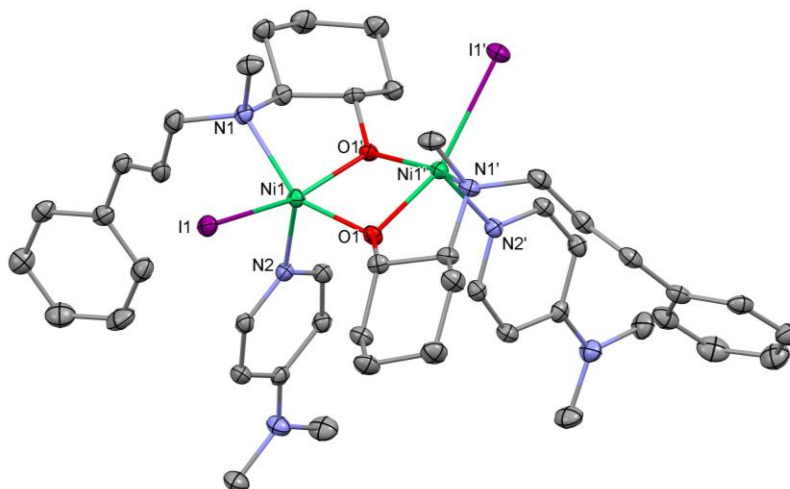


Figure S6. X-ray crystal structure of compound **6** with 50% probability ellipsoids. Co-crystallized benzene molecules and hydrogen atoms are excluded for clarity. Selected bond distances (Å) and angles (°): Ni1-I1 = 2.7099(3), Ni1-O1 = 1.9863(14), Ni1-O1' = 1.9815(14), Ni1-N1 = 2.1649(18), Ni1-N2 = 2.0405(18), N1-Ni1-O1' = 80.66(6), Ni1-O1-Ni1' = 99.50(6).

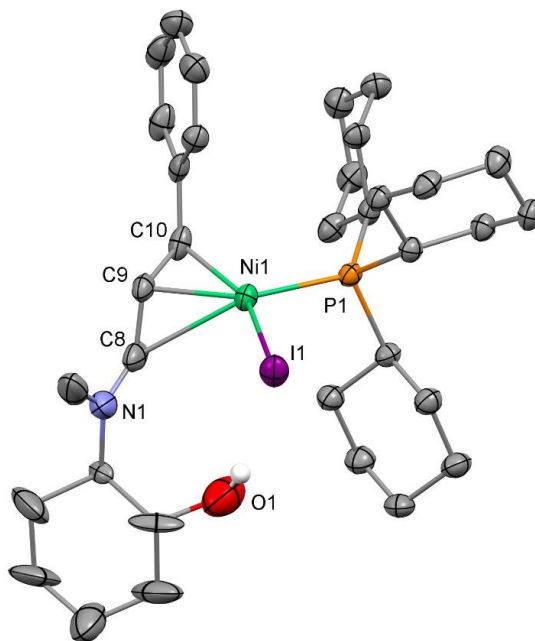


Figure S7. X-ray crystal structure of compound **7** with 50% probability ellipsoids. Hydrogen atoms (except that bound to the alcohol group) are excluded for clarity. Selected bond distances (Å) and angles (°): Ni1-I1 = 2.5476(6), Ni1-P1 = 2.1812(11), Ni1-C8 = 2.473(4), Ni1-C9 = 2.004(4), Ni1-C10 = 1.959(4), P1-Ni1-I1 = 100.33(3).

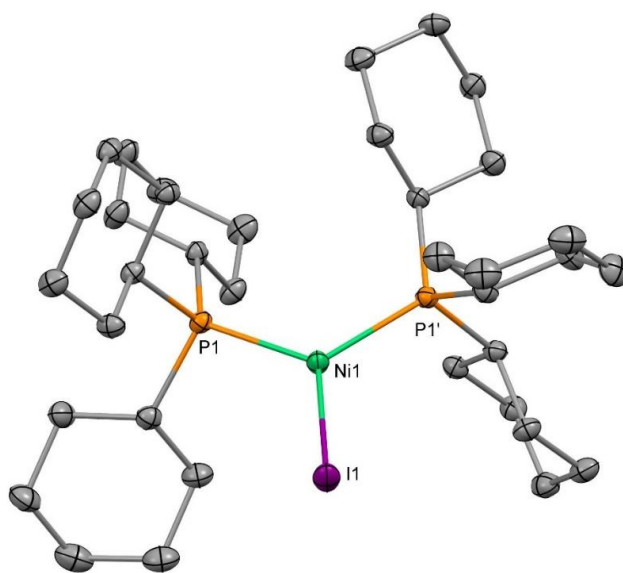


Figure S8. X-ray crystal structure of $(\text{PCy}_3)_2\text{NiI}$ with 50% probability ellipsoids. Hydrogen atoms are excluded for clarity. Selected bond distances (\AA) and angles ($^\circ$): $\text{Ni1-I1} = 2.4841(6)$, $\text{Ni1-P1} = 2.2212(7)$, $\text{P1-Ni1-P1}' = 118.45(4)$, $\text{P1-Ni1-I1} = 120.77(2)$.

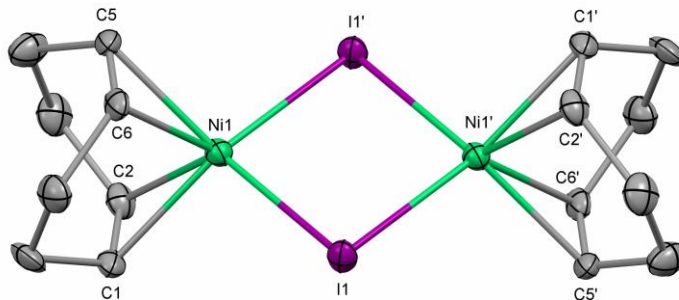


Figure S9. X-ray crystal structure of $[(\text{COD})\text{NiI}]_2$ with 50% probability ellipsoids. Hydrogen atoms are excluded for clarity. Selected bond distances (\AA) and angles ($^\circ$): $\text{Ni1-I1} = 2.6476(8)$, $\text{Ni1-I1}' = 2.6313(8)$, $\text{Ni1-C1} = 2.145(5)$, $\text{Ni1-C2} = 2.114(4)$, $\text{Ni1-C5} = 2.149(4)$, $\text{Ni1-C6} = 2.118(4)$, $\text{C1-C2} = 1.363(6)$, $\text{C5-C6} = 1.361(6)$, $\text{Ni1-I1-Ni1}' = 82.82(2)$, $\text{I1-Ni1-I1}' = 97.18(2)$.

Computational Methodologies

General Notes

All quantum mechanical calculations were carried out with the ORCA program.¹⁰ Geometry optimizations and harmonic frequency calculations were carried out with density functional theory (DFT). The PBE0 functional¹¹ paired with Becke–Johnson damped D4 dispersion corrections¹², henceforth referred to as PBE0-D4, was used. Nickel is described by the def2-TZVP all electron basis set,¹³ while all other atoms are assigned the def2-TZVP(-f) basis. Diffuse functions are added to iodine (ma-def2-TZVP(-f)), as well as the ECP28MWB small-core (25 explicit valence electrons) quasi-relativistic pseudopotential.¹⁴ This composite basis set is termed BS1. For reactions carried out in MeCN, geometry optimizations and harmonic frequency calculations were conducted with the CPCM implicit solvation model (MeCN, $\epsilon = 36.6$).¹⁵ For all calculations employing CPCM, surface charges are described by the improved Gaussian charge scheme of Neese and coworkers with a scaled Van der Waals cavity ($\alpha = 1.2$).¹⁶ Corrections for outlying charge are included in solvated energies. Gas phase geometries are used for reactions carried out in benzene. For gas phase species, the nuclear Hessians were computed analytically, while numerical Hessians were employed for solvated complexes. Stationary points are characterized by the correct number of imaginary vibrational modes (zero for minima and one for saddle points). Intrinsic reaction coordinate (IRC) analysis confirms the nature of transition states.¹⁷ Cartesian coordinates of all optimized structures are included as “.xyz” files are available online in a compressed in a zip file format.

For complexes with the tricyclohexylphosphine ligand (Cy₃P), the def2-TZVP and ma-def2-TZVP(-f) basis are used for nickel and iodine as mentioned above; however, the double- ζ split valence basis def2-SVP was employed for C, H, O, N, and P. As these complexes contain up to >140 atoms, this is necessary for the computations to remain tractable. This mixed basis set is henceforth referred to as BS3.

Electronic energies are further refined with single point calculations employing the M06 functional¹⁸ and the def2-TZVPP basis set on all atoms with additional diffuse functions on I (ma-def2-TZVPP + ECP28MWB pseudopotential). This mixed basis is henceforth referred to as BS2. Solvation was accounted for with CPCM as mentioned above (MeCN, $\epsilon = 36.6$; or benzene, $\epsilon = 2.28$). Final Gibbs free energies were obtained by applying thermodynamic

corrections obtained at the optimization level of theory to these refined electronic energies. Thermodynamic corrections from harmonic frequency calculations employ the quasi-rigid rotor harmonic oscillator approach to correct for the breakdown of the harmonic oscillator approximation at low vibrational frequencies.¹⁹ Note that free energies are adjusted to a 1 M standard state. Acetonitrile is defined to a standard state of 19.15 M for reactions run in acetonitrile ($\Delta G^{0 \rightarrow *}$ = 3.64 kcal/mol). The translational (S_{trans}) and rotational entropy (S_{rot}) contributions to the Gibbs free energy calculated for a complex in condensed phase are *ca.* 40–60% of the values obtained assuming an ideal gas.²⁰ As suggested in the literature, S_{trans} and S_{rot} obtained by ideal gas treatment are scaled by a factor of 0.5 to obtain the final condensed phase values.²¹ Hence, the final Gibbs free energy at 298.15 K is calculated as:

$$G_{\text{solv}}^* = E_{\text{el,solv}}^{\text{M06,BS2}} + \text{ZPE} + E_{\text{trans}} + E_{\text{rot}} + E_{\text{vib}} + k_b T - T \left(S_{\text{el}} + S_{\text{vib}} + \frac{1}{2} S_{\text{trans}} + \frac{1}{2} S_{\text{rot}} \right) + \Delta G^{0 \rightarrow *}$$

The resolution of identity (RI) and Chain-of-Spheres (COS) approximations are employed for efficient evaluation of Coulomb and exchange integrals, respectively.²² The def2/J auxiliary basis²³ is employed for all atoms except iodine, for which a suitable auxiliary was obtained via the automatic generation algorithm in the ORCA program (keyword: *AutoAux*).²⁴ Very fine grid settings are employed in all calculations (optimization/frequency calculations: Grid6 NoFinalGrid GridX6, single point calculations: Grid7 NoFinalGrid GridX9).

Calculations on open-shell systems employ unrestricted Kohn–Sham orbitals (UKS). Spin contamination is generally minor. Open-shell singlets are modeled using the broken-symmetry (BS) formalism. For an open-shell singlet, construction of a proper spin eigenfunction of \hat{S}^2 cannot be achieved with a single Slater determinant. As such, BS-DFT does not properly describe the open-shell singlet as a pure singlet, but rather as a mixture of the corresponding singlet and triplet states.²⁵ Various schemes for estimation of the singlet energy by removal of spin contamination have been developed. Here, we apply the formalism introduced by Yamaguchi and coworkers²⁶:

$$E_S = \frac{2(E_{BS} - E_T)}{\langle S^2 \rangle_T - \langle S^2 \rangle_{BS}} + E_T$$

Along the minimum free energy path through the catalytic cycle as described in Figure 2 of the main text, high spin (triplet) Ni(II) intermediates were also considered. These were found to be higher in energy than their singlet counterparts (Figure S10).

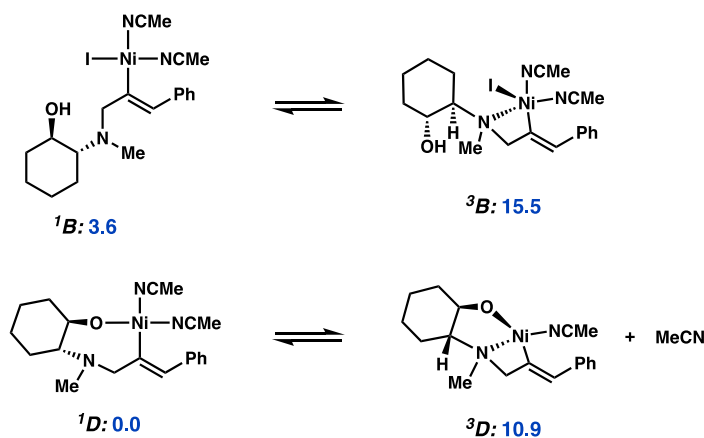


Figure S10. Relative free energies between singlet and triplet vinyl Ni(II) species.

Nucleus Independent Chemical Shift (NICS) Calculations

NICS calculations were carried out by DFT with the PBE0-D4 functional and def2-TZVP basis set in the gas phase. In accordance with literature convention, the reported NICS values are the negative of the total isotropic shift (in ppm) from the chemical shielding tensor.²⁷ The NICS value is measured at the geometric center of the ring in question. As such, a negative NICS value – additional shielding at the ring center – is indicative of a diatropic ring current, hence indicating aromaticity. Analogously, positive NICS values are obtained for antiaromatic compounds. In the ORCA code, these calculations were accomplished by placing a ghost atom at the site of interest, assigning a single Gaussian s function (one primitive, exponent = 10^6) with corresponding auxiliary to the ghost atom, and calculation of the NMR chemical shift (here using the gauge-independent atomic orbitals approach).

Table S3. NICS (in ppm) at ring centers along C–O bond formation reaction coordinates.^a

Compound	NICS (ppm)	Δ NICS (ppm)
F^{phen}	-7.19	0.00
TS(FG)^{phen}	-3.27	+3.92
G^{phen}	-6.91	+0.28
F^{cin}	-6.81	0.00
TS(FG)^{cin}	-5.02	+1.79
G^{cin}	-7.38	-0.57
F^{1nap}	-7.94	0.00
	-8.07	0.00
TS(FG)^{1nap}	-3.93	+4.01
	-7.22	+0.85
G^{1nap}	-5.59	+2.35
	-7.80	+0.27
F^{2nap}	-7.71	0.00
	-8.61	0.00
TS(FG)^{2nap}	-4.68	+3.03
	-4.80	+3.81
G^{2nap}	-5.90	+1.81
	-8.07	+0.54
benzene	-8.19	–
[benzene]²⁻	+7.80 ^b	–

^a For naphthyl rings, second value in list is from second distal aryl ring. ^b Dianion on neutral benzene geometry modeled with RKS for illustration purposes. Δ NICS defined to be NICS(transition state) – NICS(starting complex).

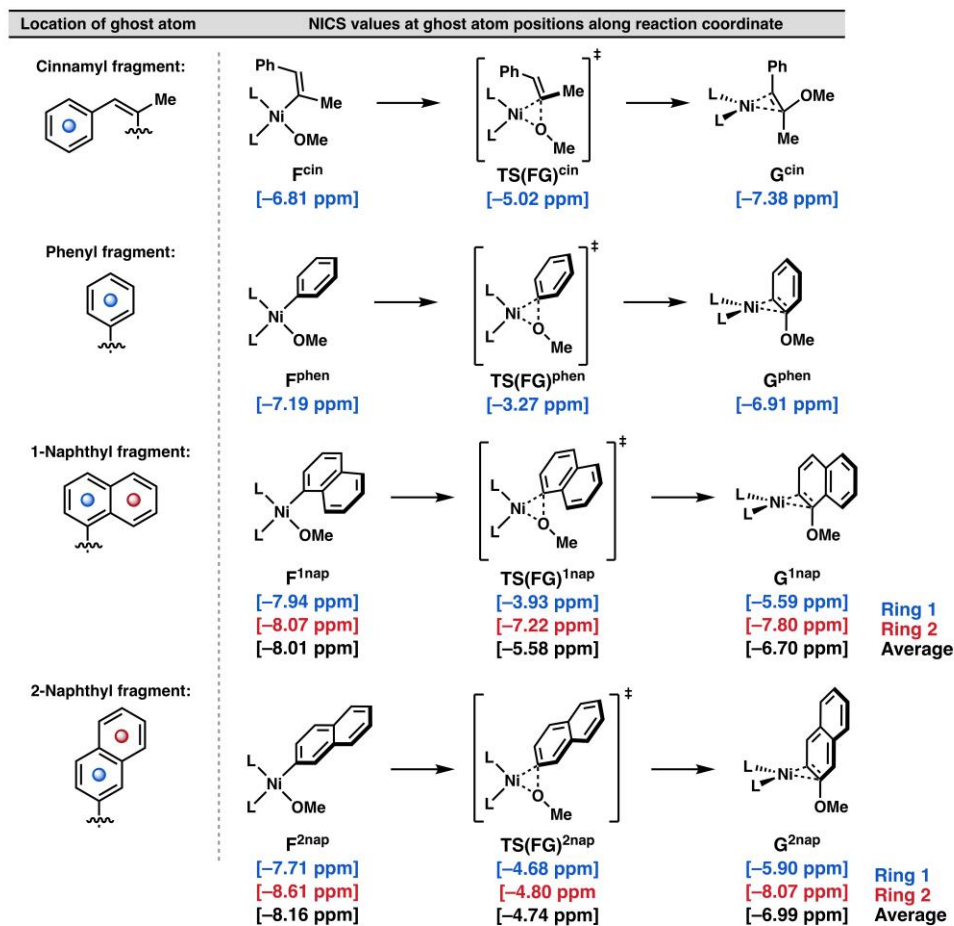


Figure S11. Schematic representation of NICS values (given in ppm) along reaction coordinate for C–O bond forming pathways.

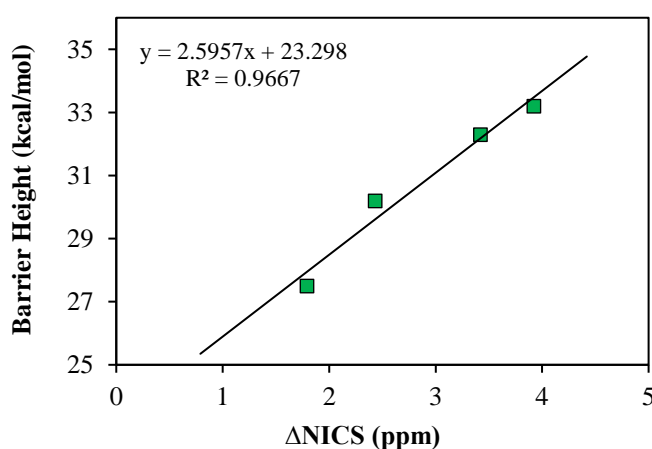


Figure S12. Plot of ΔNICS (ppm) versus calculated barrier height (kcal/mol). ΔNICS defined to be $\text{NICS}(\text{transition state}) - \text{NICS}(\text{starting complex})$. The ΔNICS value for naphthyl complexes is taken to be the average over the two aryl rings.

Coupled Cluster Calculations

Domain-based local pair natural orbital (DLPNO)-CCSD(T) calculations were performed to obtain further refined electronic energies.²⁸ Coupled cluster (CC) calculations benefit from a degree of orbital relaxation of the reference determinant by the single orbital replacements from the T_1 operator; however, the reference wavefunction should still provide a suitable basis for the coupled cluster expansion.²⁹ We consider both canonical Hartree–Fock (HF) orbitals as well as Kohn–Sham (KS) orbitals as references. The approach of using non-HF orbitals as a reference basis has been demonstrated to be particularly advantageous when the HF determinant is a less ideal zeroth order approximation for the reference state – as is often the case with transition metal complexes.³⁰ This effect has also been observed within the context of DLPNO-based CC calculations.³¹ In accord with literature findings, we observe the use of KS orbitals (BP86) in place of HF orbitals reduces the T_1 diagnostic values³² in the C–O bond forming transition states to generally ≤ 0.02 , compared to > 0.03 as obtained with HF references. The range of the T_1 diagnostic values with KS orbitals is reduced to 0.002, compared to 0.011 with HF references. As such, KS (BP86) orbitals are preferred as the reference for DLPNO-CCSD(T) calculations presented herein. We note that qualitatively similar results are obtained with both HF and KS references.

We then turned our attention to the accuracy cutoff parameters in the DLPNO-based method (T_{CutPairs} , T_{CutDO} , T_{CutPNO} , and T_{CutMKN}) as set by the keywords LoosePNO, NormalPNO, and TightPNO. While the NormalPNO settings capture the correct qualitative trends at affordable computational cost, we find deviations in barrier heights of up to 1.5 kcal/mol with respect to control calculations with the TightPNO settings (Table S4). As such, we elect to employ the TightPNO settings with BP86 reference orbitals for final energetics reported in this investigation.

Table S4. Effect of choice of reference orbitals (HF or BP86) and PNO accuracy settings (Normal/Tight) on calculated barrier heights.

Transition State	HF/Normal	HF/Tight	BP86/Normal	BP86/Tight
TS(FG) ^{vin}	28.4 [0.034]	28.1 [0.039]	30.6 [0.021]	29.3 [0.021]
TS(FG) ^{cin}	30.0 [0.028]	28.5 [0.033]	28.1 [0.021]	27.5 [0.020]
TS(FG) ^{phen}	–	33.8 [0.036]	–	33.2 [0.020]
TS(FG) ^{1nap}	–	31.5 [0.034]	–	30.2 [0.019]
TS(FG) ^{2nap}	–	33.9 [0.033]	–	32.3 [0.019]
TS(FG) ^{mc}	–	59.1 [0.028]	–	61.8 [0.019]
TS(DE)	23.2 [0.023]	22.0 [0.028]	–	21.0 [0.019]

T₁ diagnostic provided in brackets next to barrier heights (given in kcal/mol).

In the current ORCA implementation, CC amplitudes are not self-consistently optimized with respect to the solvation SCRF. As a result, solvation is taken into account by the addition of $\Delta G(\text{solv})$ calculated by DFT to gas phase CC electronic energies. $\Delta G(\text{solv})$ is calculated as $E_{\text{el}}(\text{M06/BS2/CPCM}(\text{MeCN})) - E_{\text{el}}(\text{M06/BS2})$. Hence, final Gibbs free energies are calculated as:

$$G_{\text{solv}}^* = E_{\text{el,gas}}^{\text{CC}} + E_{\text{thermo}}^{\text{DFT}} + \Delta G_{\text{solv}}^{\text{DFT}} + \Delta G^{0 \rightarrow *}$$

Comparison of density functional methods in calculation of the barrier height of the rate-determining C–O bond formation

Taking the barrier obtained by DLPNO-CCSD(T)[TightPNO/BP86]/(ma)-def2-TZVPP+ $\Delta G(\text{solv})$ as a reference value ($\Delta G^\ddagger = 21.0$ kcal/mol), we then investigated the results obtained via a variety of DFT methods for comparison. M06¹⁸, a commonly employed functionals for evaluating energetics of transition metal containing systems, performs well with a ΔG^\ddagger of 18.2 kcal/mol. Less parameterized global hybrids (B3LYP³³, PBE0¹¹) as well as Head–Gordon’s range-separated hybrid ω B97M-V³⁴ accordingly produce similar results. Surprisingly, we find MN15³⁵, parameterized to perform well across a variety of single and multi-reference systems, substantially underestimates barrier to C–O bond formation ($\Delta G^\ddagger = 15.2$ kcal/mol).

Table S5. Comparison of DFT methods for computing barrier height for C–O reductive elimination, **TS(FG)**.^a

Method	Barrier height (kcal/mol)
DLPNO-CCSD(T)	21.0
M06	18.2
PBE0-D4	18.0
B3LYP-D4	20.9
ω B97M-V	22.7
MN15 ^b	15.2

^a Calculations performed on PBE0-D4/BS1/CPCM(MeCN) geometries. The def2-TZVPP basis set and CPCM(MeCN) models are used in the final single point calculations unless otherwise specified. ^b Calculation performed using the Jaguar program with the def2-TZVPP(-g) basis set and PBF solvation model for MeCN.

Notes on the Model System

Stability of the RKS solution:

Conducting stability analysis on the RKS (PBE0/BS1/CPCM(MeCN)) wavefunction at the C–O bond forming transition states reveals instability in some cases with respect to breaking of spin symmetry – favoring the UKS broken-symmetry (BS) solution, with $\langle S^2 \rangle$ of up to 0.24. However, we find re-optimization along the broken-symmetry surface affords nearly identical geometries and final relative energies. Stability of the RKS density with respect to symmetry breaking is anticipated to be highly functional dependent. Control calculations with B3LYP-D4, M06, and PBE-D4 reveal minimal spin contamination and suggest the transition states are well described by a closed-shell KS determinant.

Table S6. Value of $\langle S^2 \rangle$ for broken-symmetry determinants (if exists) at the C–O bond forming transition states.

Transition State	PBE0-D4	B3LYP-D4	M06	PBE-D4
TS(FG) ^{vin}	0.124	0.003	0.001	0.000
TS(FG) ^{cin}	0.000	0.000	0.000	0.000
TS(FG) ^{phen}	0.243	0.030	0.010	0.000
TS(FG) ^{1nap}	0.205	0.013	0.008	0.000
TS(FG) ^{2nap}	0.209	0.014	0.007	0.000
TS(FG) ^{me}	0.000	0.000	0.000	0.000

We became curious as to whether the stability of a broken-symmetry wavefunction is an artifact of the PBE0-D4 functional or an indicator of chemically relevant non-dynamical correlation. Plotting the $\alpha - \beta$ spin density for the PBE0-D4 broken-symmetry determinant of **TS(FG)^{phen}** reveals net α spin density on Ni (predominantly in the $d_{x^2-y^2}$ orbital), with a buildup of β spin density in the π system of the phenyl ring (Figure S13). Vertical excitation energies were evaluated with time-dependent DFT (TD-DFT) calculations (B3LYP-D4/def2-TZVPP/CPCM(MeCN)) to check for low lying excited states (possibly involving the π system of the vinyl/aryl substituents) in the vicinity of the transition state. However, the lowest vertical singlet excitations [$d_{x^2-y^2}/\pi^*$ (aryl/vinyl) $\rightarrow \pi^*$ MeCN ligand] occur from 1.6 to >3.0 eV for the six transition states, with the corresponding (spin-adapted) triplets >1.0 eV above the closed-shell singlet ground state. Hence, the ground state singlet surface is well isolated from other excited states, particularly MLCT states, in the vicinity of the transition state, pointing to a suitable description within a single-reference framework. Similar TD-DFT results were obtained using the M06 functional. As discussed in the text, the aryl/vinyl π/π^* systems are indeed involved in bond formation; however, this appears to be from the aforementioned σ/π mixing rather than introduction of low-lying charge transfer excited states in the region of the TS.

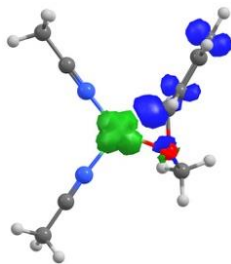


Figure S13. Plot of the $\alpha - \beta$ spin density for the PBE0-D4 broken-symmetry determinant of $\text{TS}(\text{FG})^{\text{phen}}$.

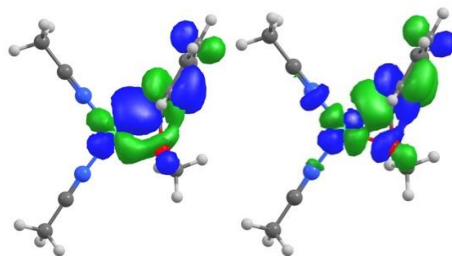


Figure S14. Ni–Ph σ/σ^* pair included in the minimal CAS(2,2) active space.

To further probe this, multiconfigurational SCF calculations were carried out using complete active space self-consistent field (CASSCF) theory, including the bonding/antibonding orbital pairs as prompted by the broken-symmetry DFT calculations (Figure S14). The natural orbitals from the resulting (2,2) active space mirror the Ni $d_{x^2-y^2}$ /phenyl π^* character of the broken-symmetry calculations. The ground state configuration interaction (CI) vector is comprised of 84% of the [20] (doubly occupied bonding) and 16% [02] (doubly occupied antibonding) configurations, indicating diradical character to be minimal. Moreover, CC calculations (vide supra) afford T_1 diagnostics of ≤ 0.021 , further suggesting an adequate single reference description.

In summary, these results suggest the dominance of a single configuration in the ground state, while highlighting the importance of the aryl/vinyl π systems in the reductive elimination process. Moreover, we expect the DLPNPO-CCSD(T) calculations with TightPNO settings and BP86 reference orbitals are well suited for evaluating the energies at these transition states.

Comparing CC to DFT in calculating barrier heights

Barrier heights calculated with M06 are systematically lower than those obtained with DLPNO-CCSD(T); however, the two methods show the same trends in reactivity (Table S7).

Table S7. DFT and CC barrier heights for C–O reductive elimination.

Transition State	M06	DLPNO-CCSD(T)
TS(FG) ^{vin}	25.4	29.3
TS(FG) ^{cin}	24.9	27.5
TS(FG) ^{phen}	28.7	33.2
TS(FG) ^{1nap}	26.8	30.2
TS(FG) ^{2nap}	28.9	32.3
TS(FG) ^{me}	53.8	61.8

Calculations performed on PBE0-D4/BS1/CPCM(MeCN) geometries. The def2-TZVPP basis set and CPCM(MeCN) models are used in the final single point calculations. DLPNO-CCSD(T) calculations employ TightPNO settings with a BP86 reference as discussed above.

C–H Bond Dissociation Energies as Metric for Disruption of π Bonding

For C–O bond formation via reductive elimination (TS(DE) and TS(FG)), the key role of σ/π mixing at the transition state in facilitating bond formation is discussed in the main text. The degree of stabilization experienced at the transition state depends on the ability of the ligand-based π^* to serve as an acceptor in the HOMO/LUMO mixing. For example, **F^{vin}** undergoes reductive elimination more readily than **F^{phen}**, as partially occupying the phenyl π^* is detrimental to the resonance stabilization of the π system of the aryl ligand, whereas this does not apply to the vinyl π system. Above, we investigate this from the viewpoint of NICS. Here, we the energetic cost of breaking a C=C bond by virtue of the ability for a π system to accept H \cdot , generating the corresponding radical. We define C–H bond dissociation energy (BDE) to be the change in electronic energy from the organic radical to the closed-shell π system and H \cdot (the reverse of the process stated above). A high C–H BDE indicates less penalty for breaking the C=C bond (Figure S15). A lower energetic penalty for lowering the bond order of the π system would correlate with a more facile σ/π mixing at the transition state (in which the ligand π^* serves as an acceptor to a M–L σ donor). As hypothesized, a correlation between C–H BDE and barrier height for C–O reductive elimination exists (Figure S16).

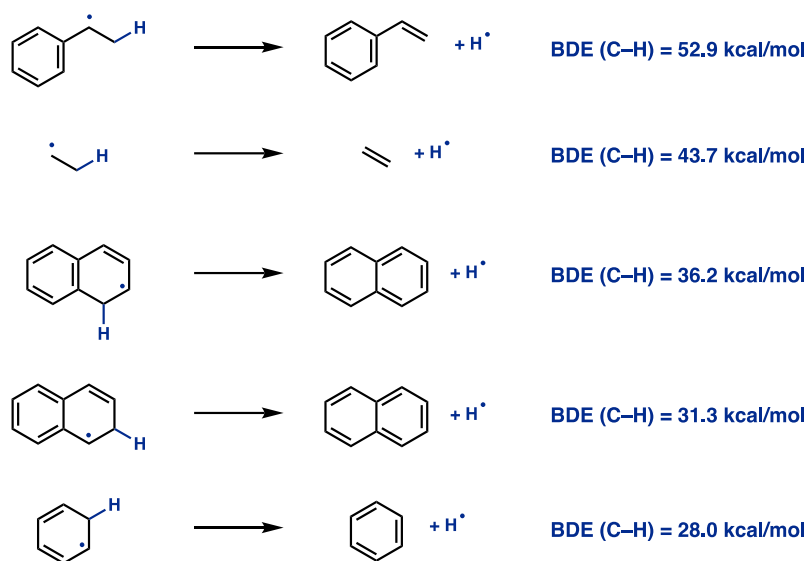


Figure S15. C-H bond dissociation energy (BDE) from organic radical compounds (in kcal/mol). Calculated at the PBE0-D4/def2-TZVP(-f) level of theory.

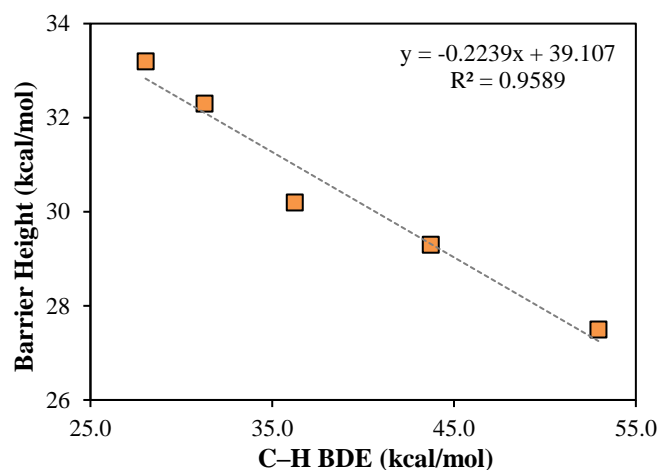


Figure S16. Plot of barrier height to C-O reductive elimination from Ni(II) complexes **F** versus C-H bond dissociation energy (BDE), in kcal/mol, from organic radical compounds corresponding to the C(sp²) fragments of complexes **F**.

Oxidative Addition Mechanisms

In the minimum free energy path presented in Figure 2 of the main text, four mechanisms of oxidative addition from **A** to **B/C/D** are considered³⁶: (1) A three-centered transition state leading to **B**, (2) an anti-displacement-type mechanism leading to cationic Ni(II) intermediate **C**, (3) halide abstraction affording a Ni(I) iodide and organic radical, and (4) outer-sphere electron transfer, followed by radical recombination (Figure S17). With an apparent barrier height of 10.3 kcal/mol, anti-displacement (**TS(BC)**) represents the lowest energy pathway for C–I bond cleavage. Oxidative addition via a canonical three-centered transition state is competitive, with a ΔG^\ddagger of 13.5 kcal/mol. As a control, geometries were also obtained in the gas phase. These calculations slightly favor the less polar three-centered transition state. Halide abstraction (**TS(HI)**) proceeds with a higher barrier of 22.8 kcal/mol. Tris(acetonitrile) complexes were also considered.

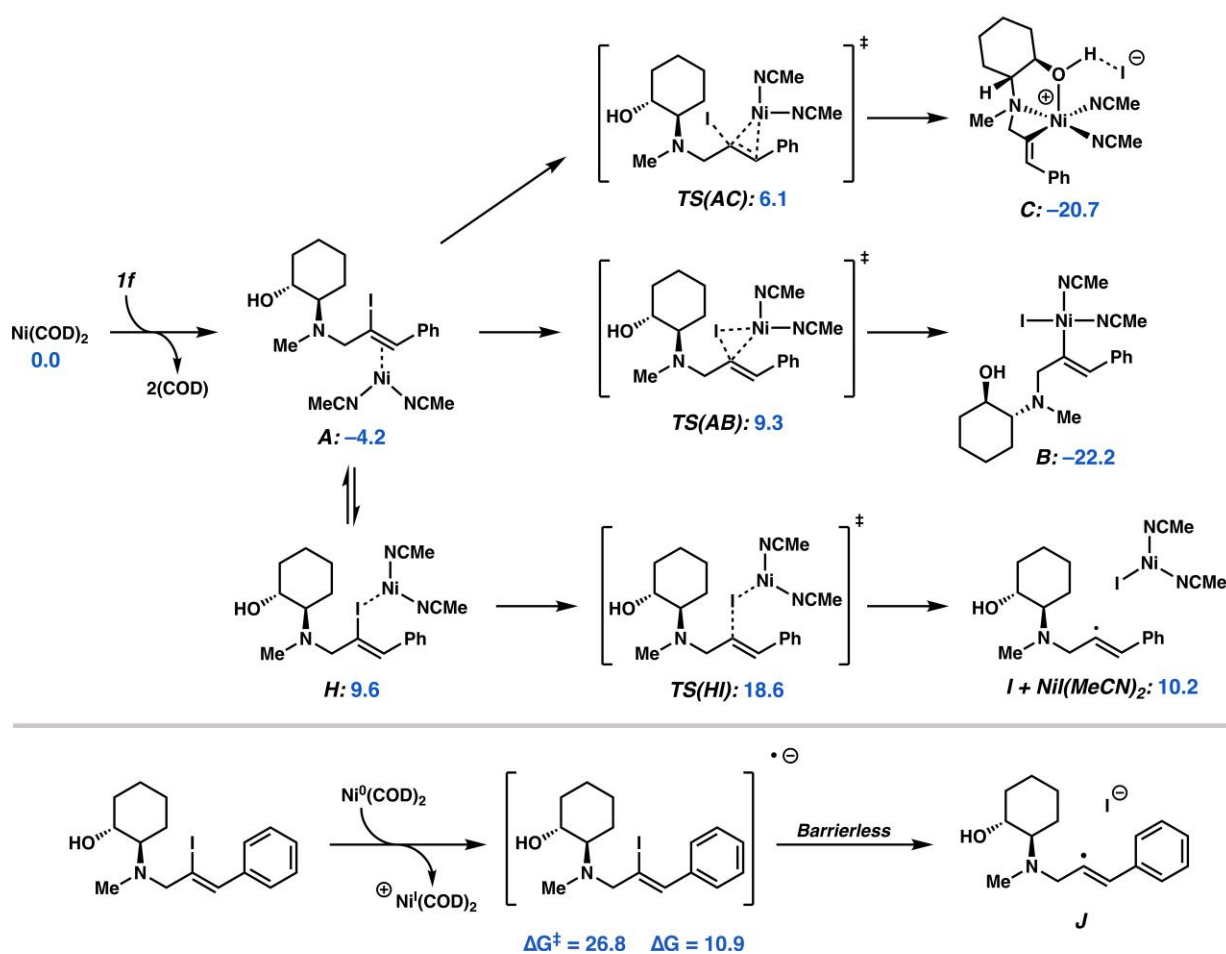


Figure S17. Oxidative addition mechanisms considered herein.

The barrier height for outer-sphere electron transfer is evaluated by Marcus theory. Vertical reorganization energies (λ) approximated by Nelsen's four-point model using electronic energies at the M06/BS2/CPCM(MeCN) level of theory (Figure S17).³⁷ Hence, reorganization energy is calculated as the electronic energy of the initial state ($\mathbf{D}+\mathbf{A}$) at the optimized geometry of the initial state ($\mathbf{D}+\mathbf{A}$) subtracted from the electronic energy of the initial state ($\mathbf{D}+\mathbf{A}$) at the geometry of the final state ($\mathbf{D}^{*+}+\mathbf{A}^{*-}$). Change in free energy (ΔG^0) is calculated at the M06/BS2/CPCM(MeCN)//PBE0-D4/BS1/CPCM(MeCN) level of theory. Note that single electron reduction of substrate **1f** leads to concomitant cleavage of the C–I bond to afford a C-centered radical and iodide (Figure S17).

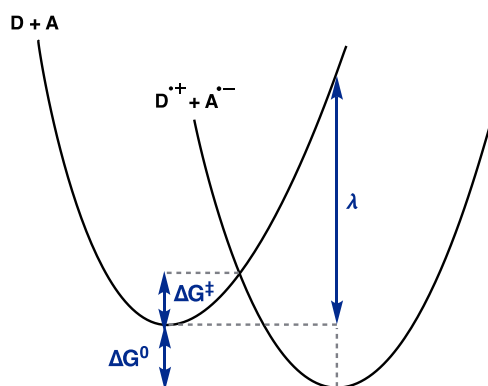


Figure S18. Model reaction coordinate for outer-sphere electron transfer.

The corresponding free energy barrier is calculated as:

$$\Delta G^{\ddagger} = \frac{(\lambda_0 + \Delta G^0)^2}{4\lambda_0}$$

A reorganization energy (λ) of 83.9 kcal/mol paired with a reaction free energy (ΔG^0) of 10.9 kcal/mol affords ΔG^{\ddagger} of 26.8 kcal/mol.

Thermodynamics of reorganization to π -allyl complex **M**

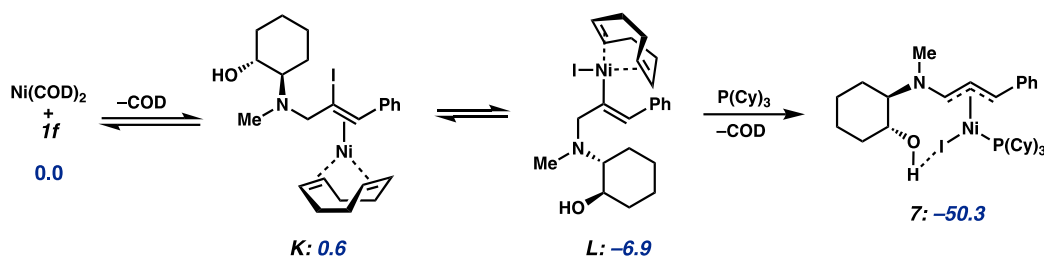


Figure S19. Free energy change for the reaction of Ni(COD)_2 and substrate **1f** to give π -allyl complex **7**. Gibbs free energies give in kcal/mol at the M06/(ma)-def2-TZVPP/CPCM(Et_2O)/PBE0-D4/BS3 level of theory.

In stoichiometric experiments, pre-mixing PCy_3 and Ni(COD)_2 followed by addition of **1f** yields predominantly halide abstraction, producing $(\text{PCy}_3)_2\text{NiI}$ (see Figure 7 and 8 in the main text). We suspect this is due to the formation of sterically encumbered PCy_3 -ligated Ni(0) complexes which undergo halide abstraction with **1f** preferentially to $2e^-$ oxidative addition (see Figure 8 in main text). Instead, if substrate **1f** is first reacted with 1 equivalent of Ni(COD)_2 followed by addition of PCy_3 , π -allyl complex **7** is formed. As such, we suspected that Ni(COD)_2 undergoes facile oxidative addition with **1f** and the resultant Ni(II) vinyl iodide **L** is thermodynamically preferred to its Ni(0) precursors. Our computations corroborate this hypothesis, finding the formation of Ni(II) vinyl iodide **L** is accompanied by a free energy change of -6.9 kcal/mol (Figure S19). In the absence of a vinyl iodide or base with zinc (II) salts, treatment of intermediate **L** with PCy_3 affords π -allyl complex **7** with a ΔG of -50.3 kcal/mol.

Despite extensive efforts, starting from the crystallographic structure of **7**, optimizations at the PBE0-D4/BS3 level of theory return one small imaginary mode (<100 cm^{-1}) corresponding to the rocking of the ally group/ Ni center. Control optimizations and Hessian calculations with PBE-D4/BS3 level of theory afford nearly superimposable structures with no imaginary modes. Regardless, these observations bear no effect on the final conclusions.

Disproportionation from Ni(II)/Ni(II) to Ni(I)/Ni(III)

We have further investigated the possibility for a disproportionation event between two Ni(II) species to give Ni(I) and Ni(III) intermediates. From the catalyst resting state (**D**) in MeCN, outer-sphere electron transfer affords anionic Ni(I) and cationic Ni(III) intermediates **M** and **N**, respectively. Geometric relaxation and solvent exchange afford a ΔG of 41.5 kcal/mol,

disfavoring the formation of the Ni(I)/Ni(III) products (Figure S20). Although already 3.6 kcal/mol higher in energy than the resting state (**D**), disproportionation from Ni(II) iodide complex **B** was also considered. Even allowing anion exchange for charge equilibration, disproportionation to Ni(I) and Ni(III) complexes **O** and **P** is disfavored by 53.6 kcal/mol. Note that the lowest energy isomers and ligation environments are depicted. In summary, disproportionation from Ni(II)/Ni(II) to Ni(I)/Ni(III) is thermodynamically inaccessible. These results are in accord with prior literature.³⁸

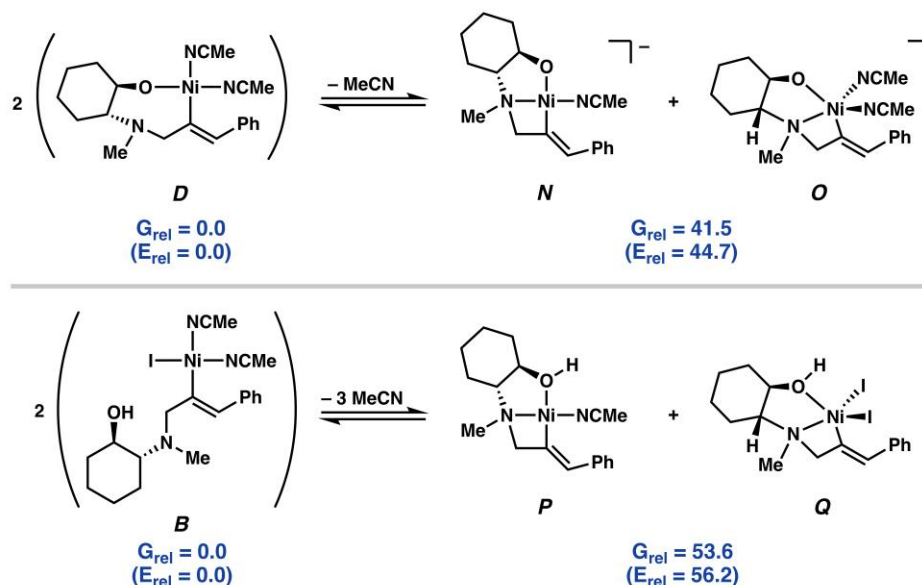
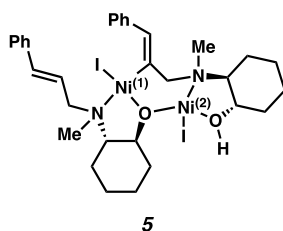


Figure S20. Thermodynamics of disproportionation of Ni(II)/Ni(II) to Ni(I)/Ni(III) from Ni(II) intermediates **B** and **D**. Energies referenced from 2 mol Ni(II) to 1 mol Ni(I) plus 1 mol Ni(III).

Electronic structure of dinuclear Ni complex **5**



Complex **5** is a dinuclear nickel species bearing a square planar nickel center ($\text{Ni}^{(1)}$) and a distorted tetrahedral nickel ($\text{Ni}^{(2)}$) center. Given the ligand field environment, **5** was anticipated to present a triplet ground state with both nickel centers formally in the (II) oxidation state and with $\text{Ni}^{(2)}$ in a high spin configuration. An effective magnetic moment (μ_{eff}) of 3.57 B.M. (with $\text{Ni}^{(2)}$ in a high spin configuration).

diamagnetic correction) is found via Evan's method (see text). This is consistent with the presence of one high spin Ni(II) center. We sought to further explore the spin state assignment of **5** by computational analysis. The X-ray crystal structure of **5** contains a Ni-bound molecule of THF which hydrogen bonds to the pendant alcohol coordinated to Ni⁽²⁾. Elemental analysis of the bulk material suggests the THF molecule is indeed an artifact of subsequent crystallization conditions (THF/hexanes) employed for obtaining X-ray quality crystals. (Note that bulk **5** is isolated without exposure to THF). Indeed, when THF is present a ΔG of 1.0 kcal/mol is calculated favoring the formation of **5**•THF from **5** and THF (Figure S21).

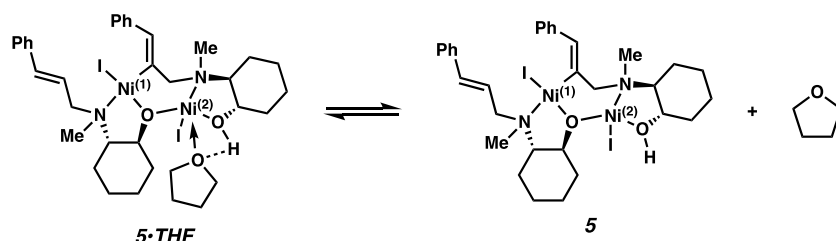


Figure S21. Coordination of THF to **5** to give **5**•THF is favorable by 1.0 kcal/mol.

To obtain a representative structure of **5**, the Ni-bound molecule of THF was removed from the complex and the coordinates were relaxed. This was performed for the lowest energy closed-shell singlet (CSS), open-shell singlet (OSS), triplet, and quintet states. The optimization was carried out with DFT using the PBE0-D4 functional with the def2-TZVP basis set for Ni, ma-def2-SVP with ECP28MWB small-core pseudopotential for iodine, and def2-SVP for all other atoms. Single point calculations were then carried out on **5** at the M06/BS2/CPCM(benzene) level of theory for the lowest singlet, triplet, and quintet spin states. The triplet (low spin at Ni⁽¹⁾ and high spin at Ni⁽²⁾) is lowest in energy with the CSS [two low spin Ni(II)], OSS [antiferromagnetically-coupled high spin Ni(II) centers], and quintet [two high spin Ni(II)] at 15.4, 13.9 and 13.9 kcal/mol higher in energy, respectively. While bond distances and angles vary, the ligation of **5** remained the same across the relaxed geometries in different electronic configurations. The coordinates for all four complexes are available in the coordinate data file, labeled as **5**, **5_CSS**, **5_OSS**, and **5_HS**. For high-spin Ni(II) centers, Löwdin spin populations of 1.603–1.570 were found (lower than the value of 2 from Ni–L covalency – the unpaired spin-bearing orbitals, d_z^2 and $d_{x^2-y^2}$, have character on ligating atoms) (Table S8). Analysis of intrinsic atomic orbitals (IAOs)³⁹ reveals 13 α and 13 β spin electrons are localized

to Ni⁽¹⁾, while 14 α and 12 β spin electrons are localized to Ni⁽²⁾. These results further corroborate the formal oxidation state assignments in complex **5** as two Ni(II) centers, Ni⁽¹⁾ low spin and Ni⁽²⁾ high spin.

Table S8. Löwdin atomic spin populations for **5** optimized in different spin states.^a

Complex	Löwdin spin population on Ni ⁽¹⁾	Löwdin spin population on Ni ⁽²⁾	$\langle \hat{S}^2 \rangle$
5	0.024	1.603	2.238
5_CSS	0.000	0.000	0.000
5_OSS^b	1.573	-1.571	2.021
5_HS	1.566	1.570	6.023

^a Löwdin atomic spin populations and $\langle \hat{S}^2 \rangle$ calculated with M06/BS2/CPCM(benzene). ^b Net α - β signed spin density for an OSS is a consequence of the broken-symmetry formalism, i.e. the necessarily improper description of open-shell singlet states by a single Slater determinant. The opposite signed α - β spin density and each Ni center indicates the desired “OSS” state (broken-symmetry state) was captured, however we remind the reader that a α - β spin density for a proper singlet state is unphysical as a pure singlet state is defined as having $\langle \hat{S}^2 \rangle = 0$.

While these results suggest a ground state with formally Ni(II)/Ni(II) oxidation states, we were curious as to whether facile electron transfer could occur between the nickel centers to afford a Ni(I)/Ni(III) species. Time-dependent density functional theory (TD-DFT) calculations were carried out from the triplet ground state of **5** with the M06/BS2/CPCM(benzene) level of theory. The first 12 excitations (0.48–2.00 eV) are d-d excitations within the ligand field of single nickel centers. The first inter-nickel charge-transfer (CT) excitation found is at 2.16 eV and is characterized by CT from Ni⁽¹⁾/L to Ni⁽²⁾. Natural Transition Orbitals (NTOs) were utilized in this analysis. The NTO donor/acceptor pair describing 99% of the transition ($n = 0.990$) character is depicted below (Figure S22). Note that the donor NTO has significant character on the iodine ligand on Ni⁽¹⁾. While the TD-DFT description of the energetics of CT states is often not quantitatively accurate, these initial calculations qualitatively highlight the significant preference for the Ni(II)/Ni(II) configuration over Ni(I)/Ni(III).

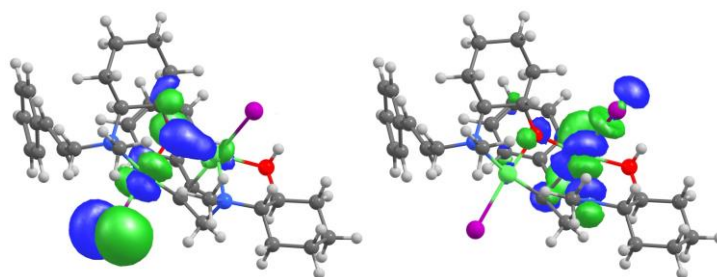


Figure S22. Donor (left) and acceptor (right) NTOs for 12th root.

Thermodynamics of the formation of complexes **6** and **7**

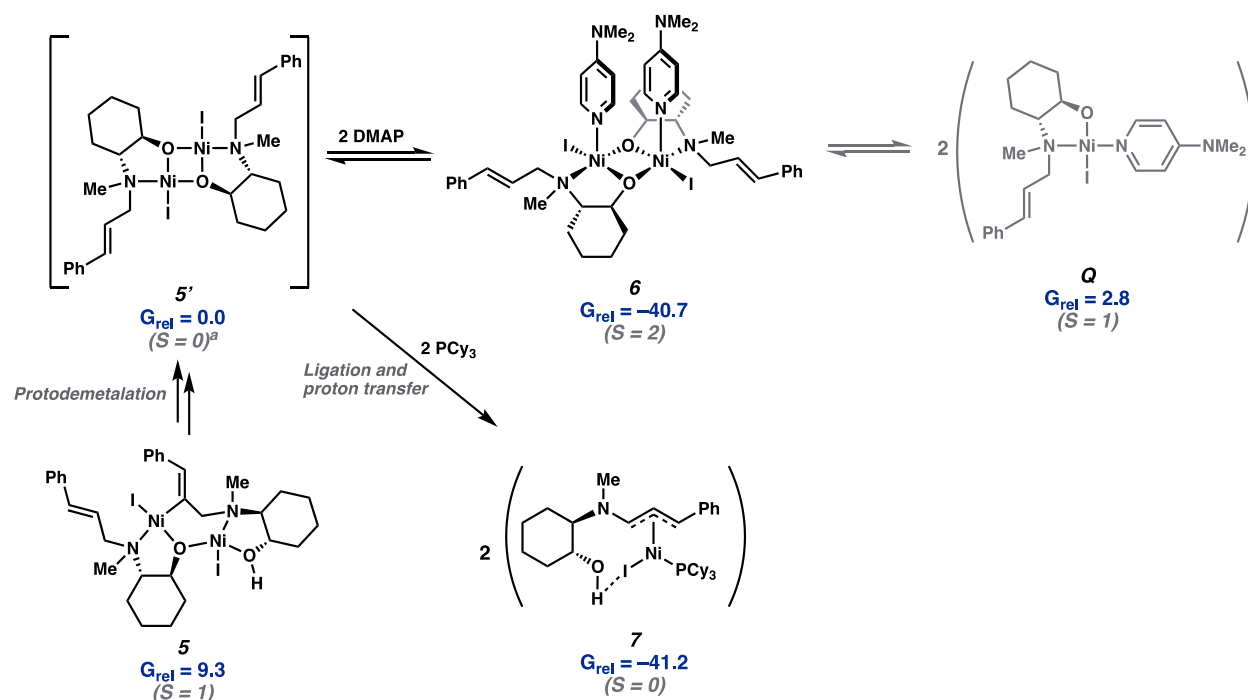


Figure S23. Relative free energies in kcal/mol for dinuclear and mononuclear intermediates formed in non-coordinating solvents obtained as described above.

Complex **6** is high spin ($S = 2$) in the ground state. The open-shell singlet (antiferromagnetically-coupled high spin Ni(II) centers) and closed-shell singlet are found to be 3.7 and 30.3 kcal/mol higher in energy than the high spin complex. As with **5**, the relaxed geometries for each spin state are available in the structure data file (**6**, **6_CSS**, and **6_OSS**).

Given the small difference in energy between the high spin and low spin states of **5'**, the assignment of spin state becomes increasingly dependent on the method employed. B3LYP-D4 and M06-L find the singlet and triplet state complexes to be less than 0.5 kcal/mol different in

energy. PBE0-D4 affords a preference of 6.5 kcal/mol for the low spin **5'** while M06 and TPSSh predict a closed-shell singlet by 8.2 and 8.3 kcal/mol (Table S9). These calculations highlight the known challenges of computing energy differences between different spin states in transition metal complexes. Regardless, we find the subsequent formation of DMAP and PCy₃ adducts **6** and **7** to be highly thermodynamically favorable and their formations from **5/5'** irreversible.

Table S9. Comparison of relative energies of high-spin and low-spin **5'** computed across different density functionals.

Method	Low-spin R	High-spin R
PBE0-D4	6.5	0.0
B3LYP-D4	0.0	0.3
M06-L	0.0	0.4
M06	0.0	8.2
TPSSh	0.0	8.3

Acid/Base equilibrium and importance of Zn(II) salt additives

Throughout our experimental and computational investigations, we find that Zn(II) salts play an important role in sequestering iodide produced after oxidative addition. These may be produced either from reduction of sacrificial Ni iodide species or from the reaction of Zn⁰ with the HI formed in the reaction after oxidative addition. Modeling the exact speciation of Zn(II) salts in the reaction is challenging and this matter is further complicated by (in)solubility of some of these potential adducts. Likewise, Zn(OTf)₂ is used in the modified reaction conditions due to its improved solubility over ZnI₂. For simplicity, we highlight in a general case how solvated ZnI₂ may aid in sequestration of iodide through formation of zinc-ate (ZnI₄²⁻) derived intermediates. The computed ΔG of -29.5 kcal/mol for formation of [Et₃NH]₂ZnI₄ from ZnI₂ and Et₃NHI demonstrates this point (Figure S24). The corresponding process with Zn(OTf)₂ should be similar, if not even more favorable.

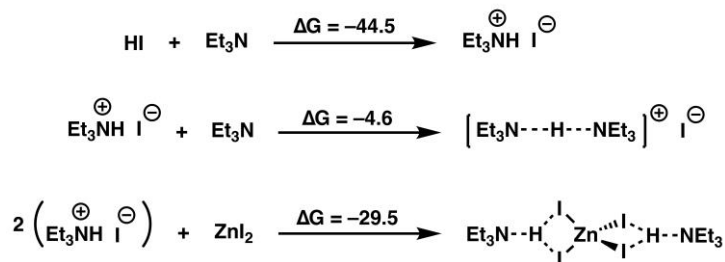


Figure S24. Impact of ZnI₂ on sequestration of iodide and formation of stable adducts.

Alternative C–O bond forming mechanistic hypotheses

Throughout the course of our investigation numerous mechanistic hypotheses were considered for C–O bond formation. While in the full context of experimental and computational investigation it is now clear that π -allyl complex **7** is not catalytically relevant, we initially suspected C–O bond formation may occur from nucleophilic attack of the electrophilic β carbon of the π -allyl moiety (Figure S25). Our initial investigations highlight a thermodynamic preference of 13.8 kcal/mol for π -allyl intermediate **R** over metallacyclobutane **S**. Critically, given the geometric constraints of **S**, β -hydride elimination is not anticipated to be facile. Accordingly, a barrier of 32.0 kcal/mol is found for this step (**TS(ST)**). Note that high spin **S** was found to have a relative free energy of 39.8 kcal/mol. These preliminary results we obtained with the PBE-D4/def2-TZVP [Ni], ma-def2-SV(P) [I], def2-SV(P) level of theory.

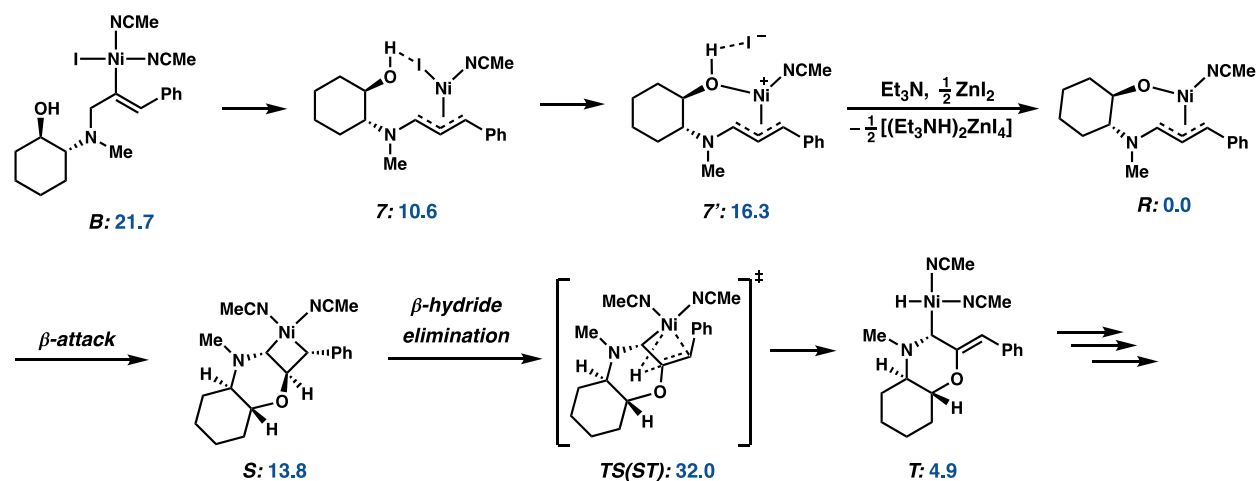
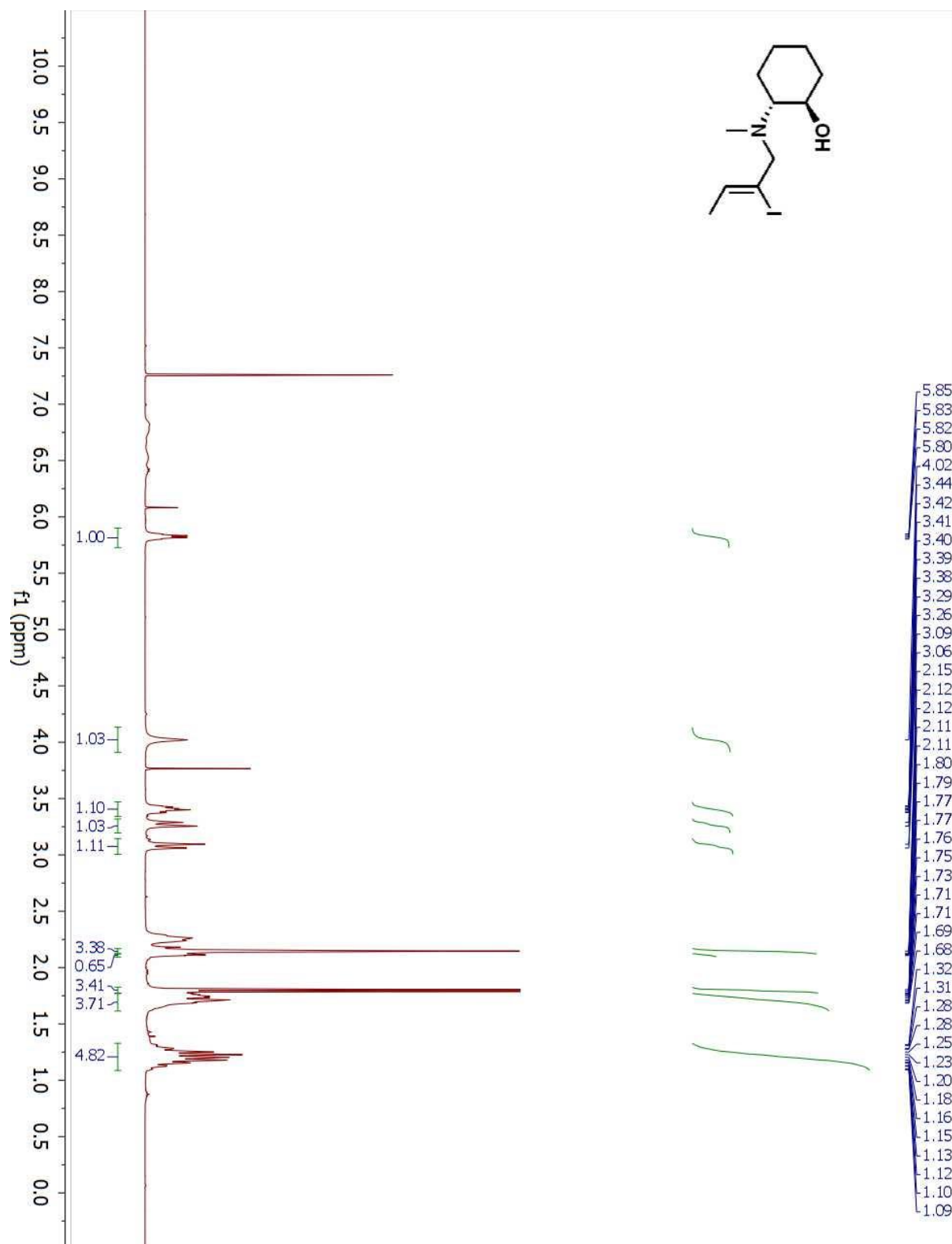


Figure S25. Alternative mechanistic hypothesis for C–O bond formation. Relative free energies given in kcal/mol.

An oxa-Heck type mechanism was also considered starting from a protodemetalated olefin. *Syn*-addition of a nickel alkoxide can be eliminated on a basis of stereochemical outcome of the observed product – the enol ether after subsequent β -hydride elimination would bear the *E* olefin geometry when starting from the *Z* styrene. The charge separated intermediates required for an *anti*-addition are found to be high in energy or unstable on the PES. When olefin **3** is subjected to the reaction conditions (with or without strong exogenous base), no productive reaction is experimentally observed.

NMR Spectra of New Compounds and Key Experiments

Figure S26. ¹H NMR spectrum of **1a** in CDCl₃.

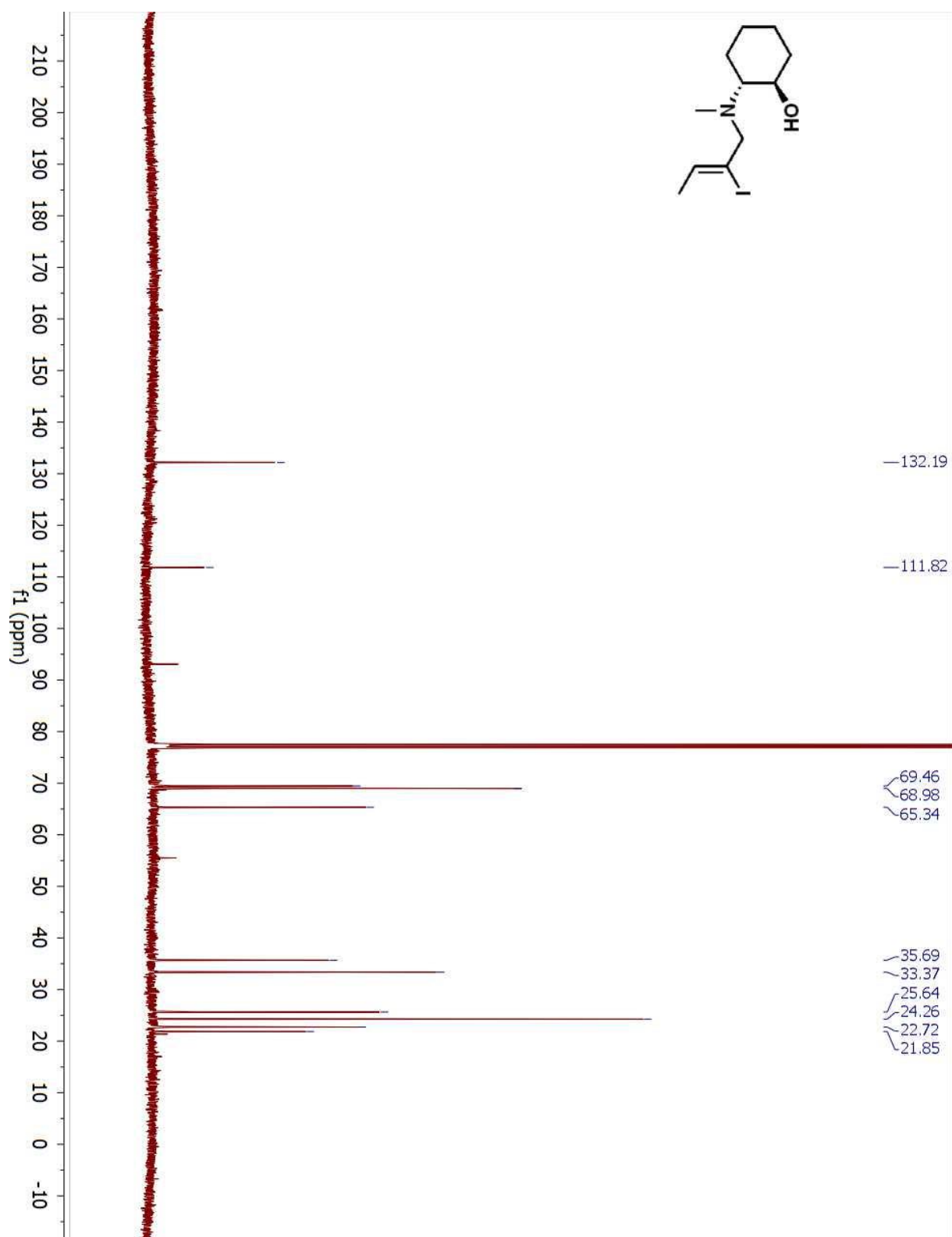


Figure S27. ^{13}C NMR spectrum of **1a** in CDCl_3 .

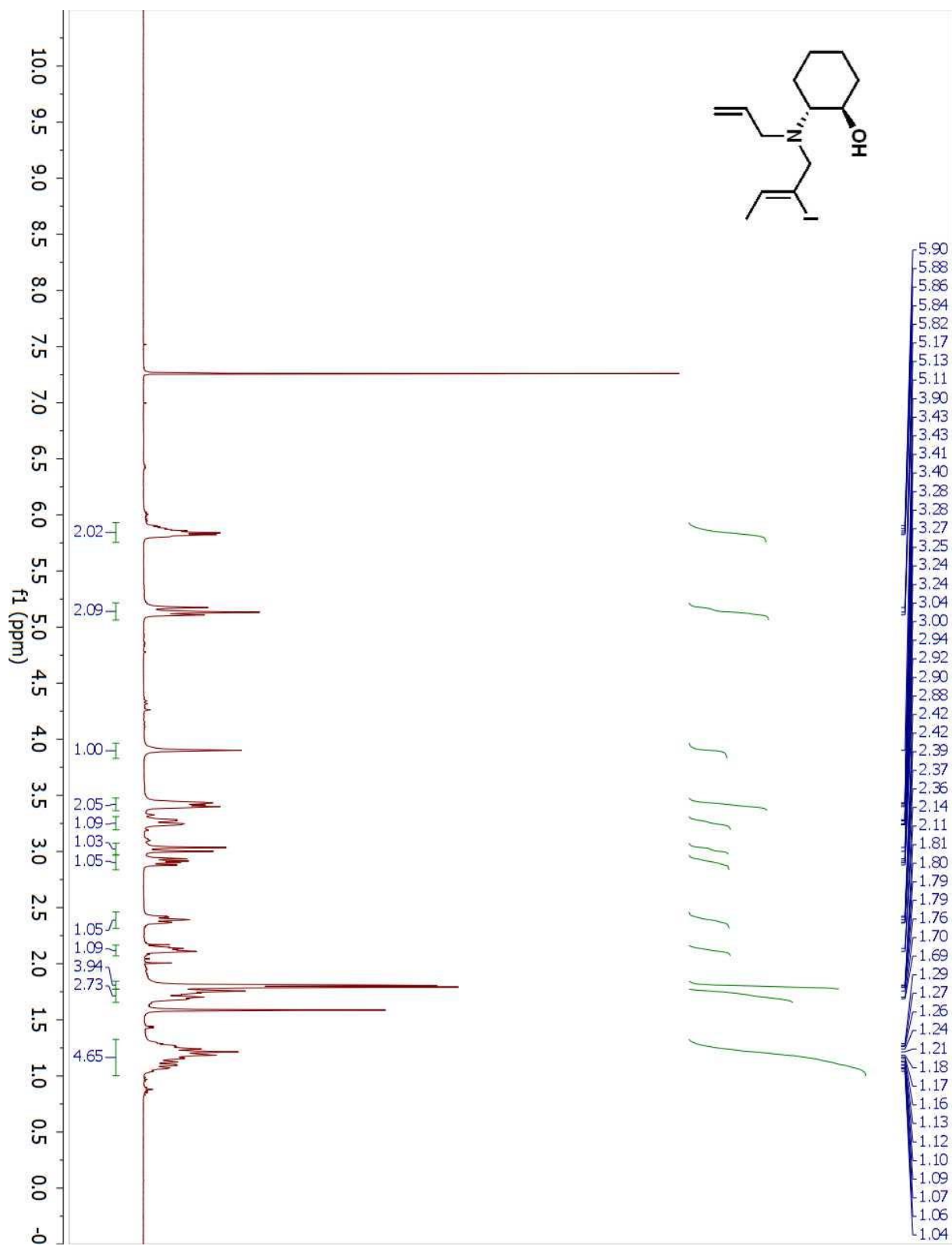


Figure S28. ^1H NMR spectrum of **1d** in CDCl_3 .

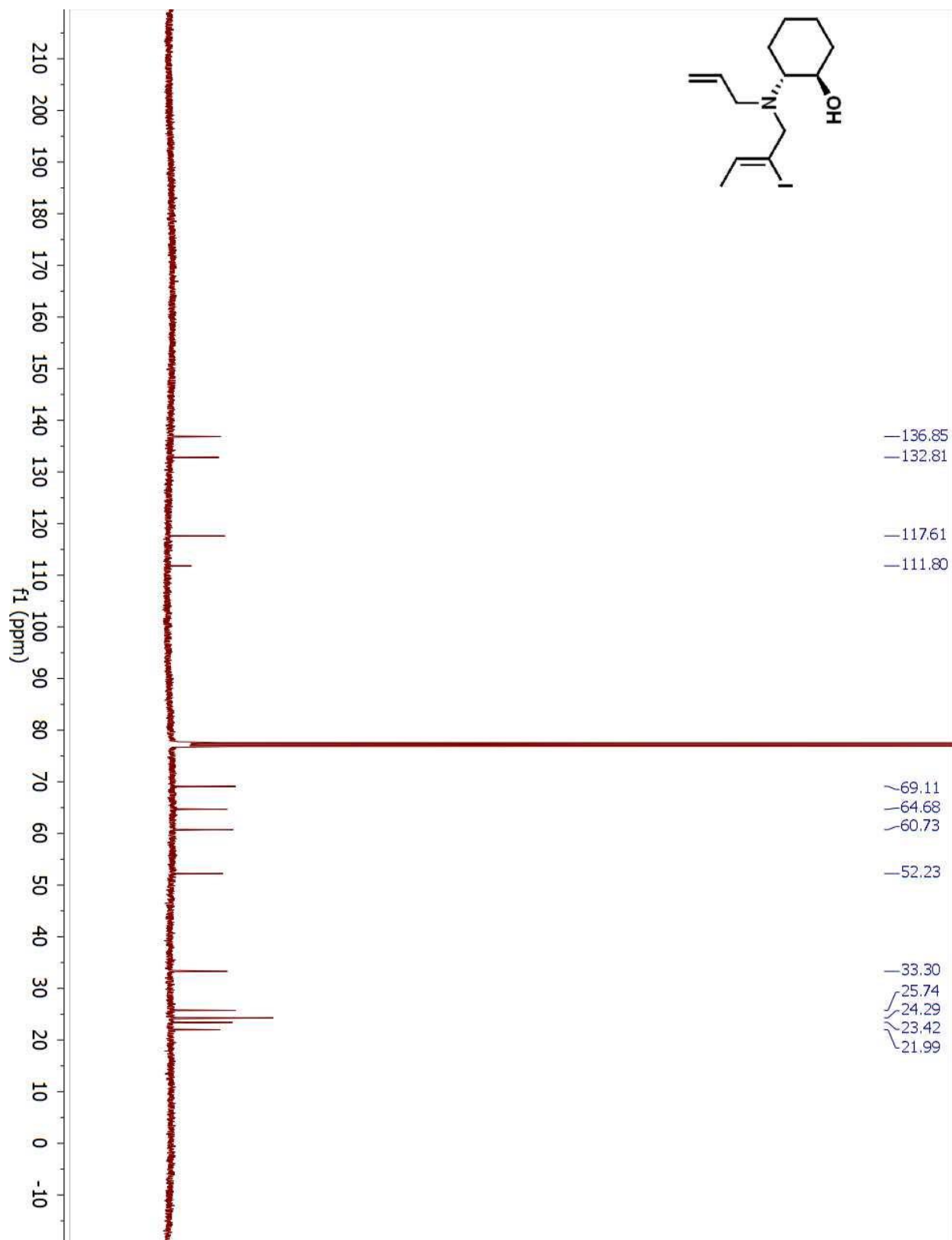


Figure S29. ^{13}C NMR spectrum of **1d** in CDCl_3 .

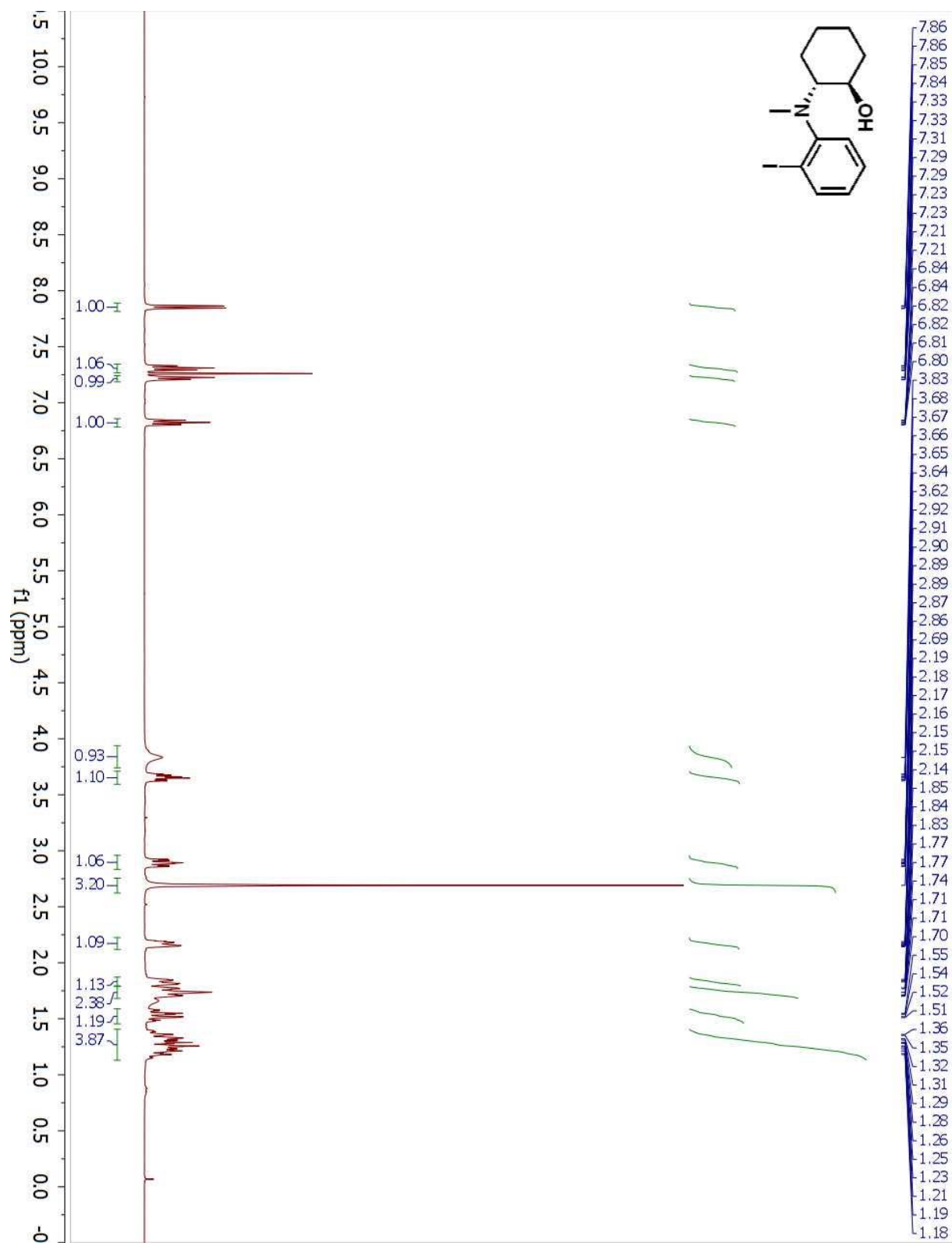


Figure S30. ^1H NMR spectrum of **1e** in CDCl_3 .

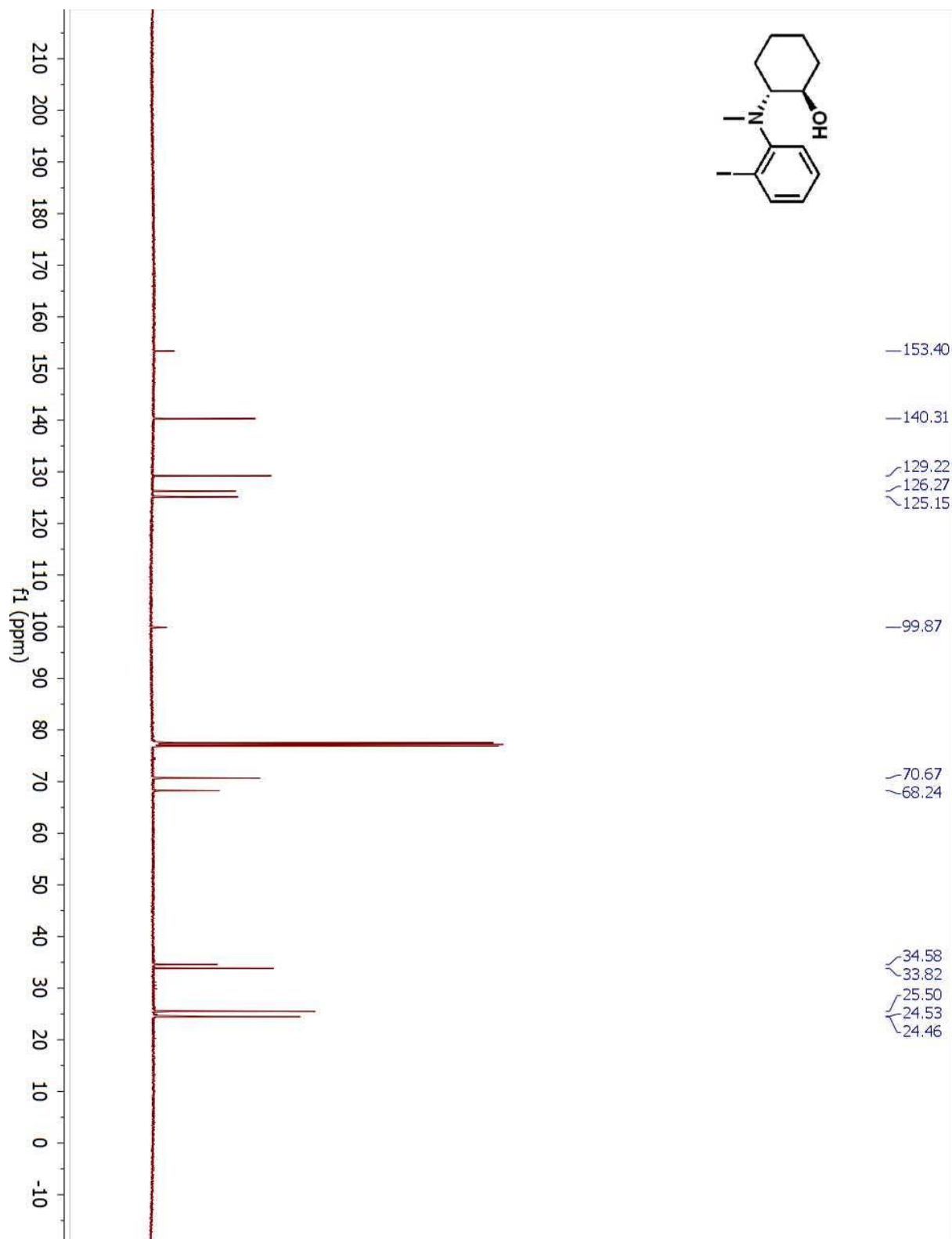


Figure S31. ^{13}C NMR spectrum of **1e** in CDCl_3 .

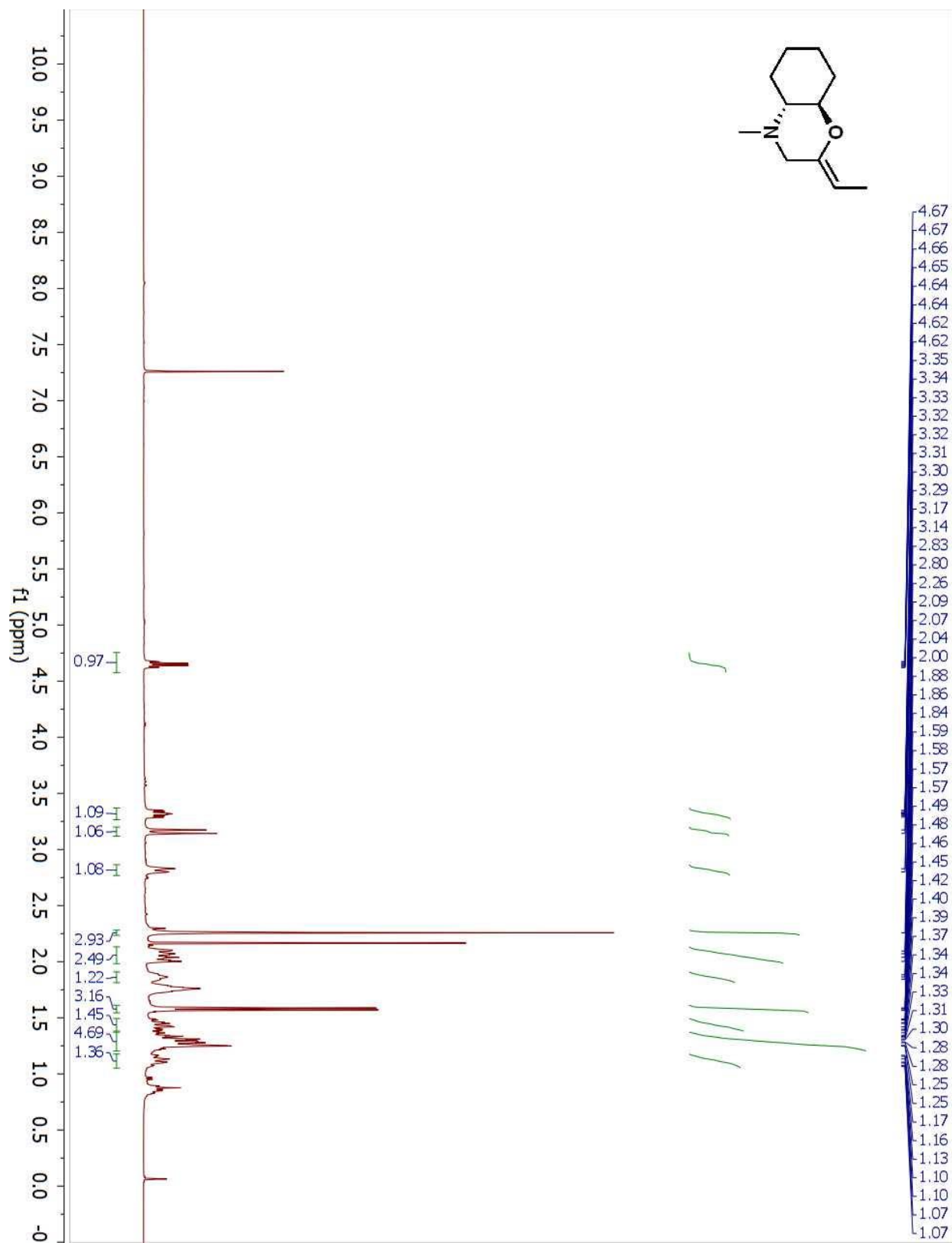


Figure S32. ^1H NMR spectrum of **2a** in CDCl_3 .

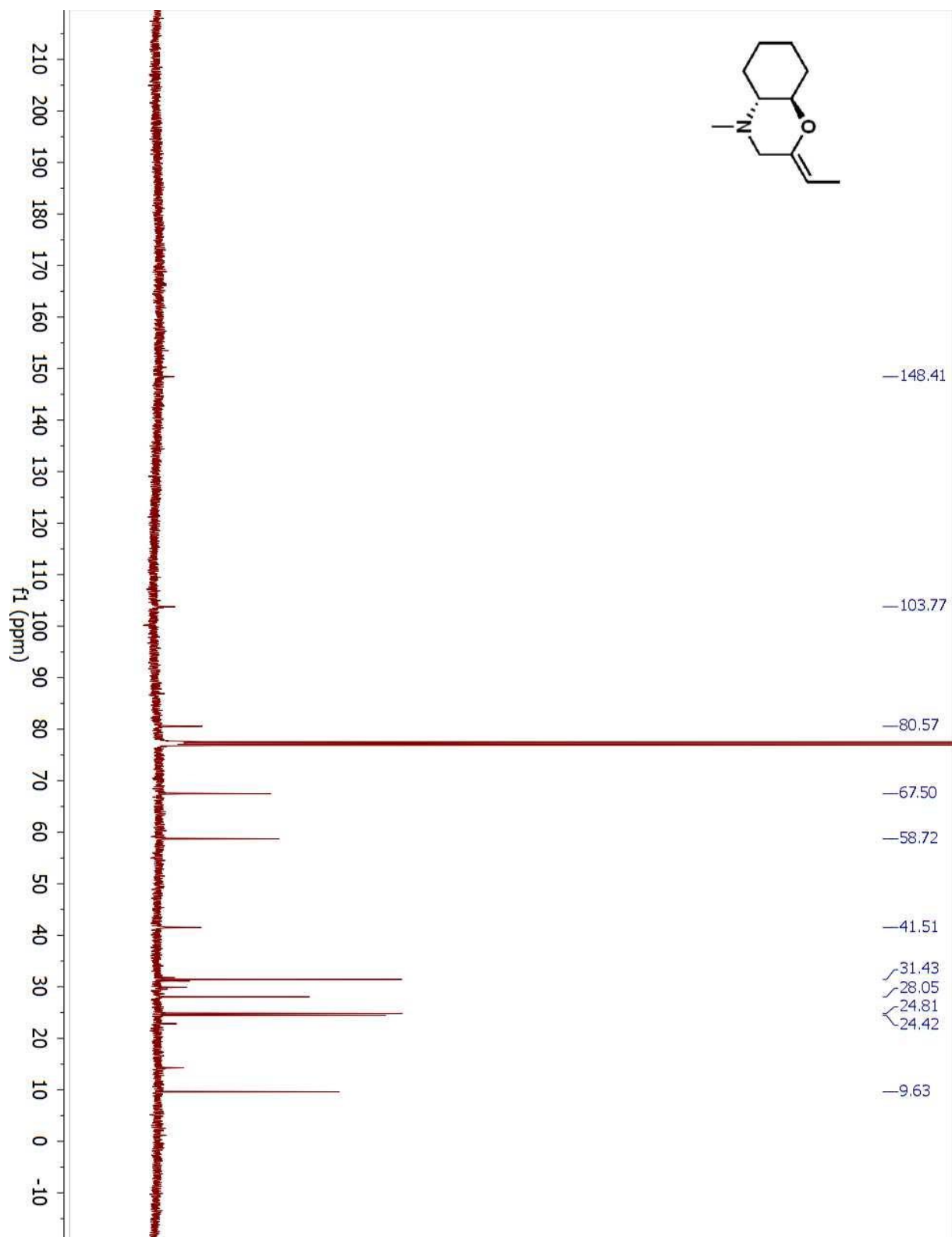


Figure S33. ^{13}C NMR spectrum of **2a** in CDCl_3 .

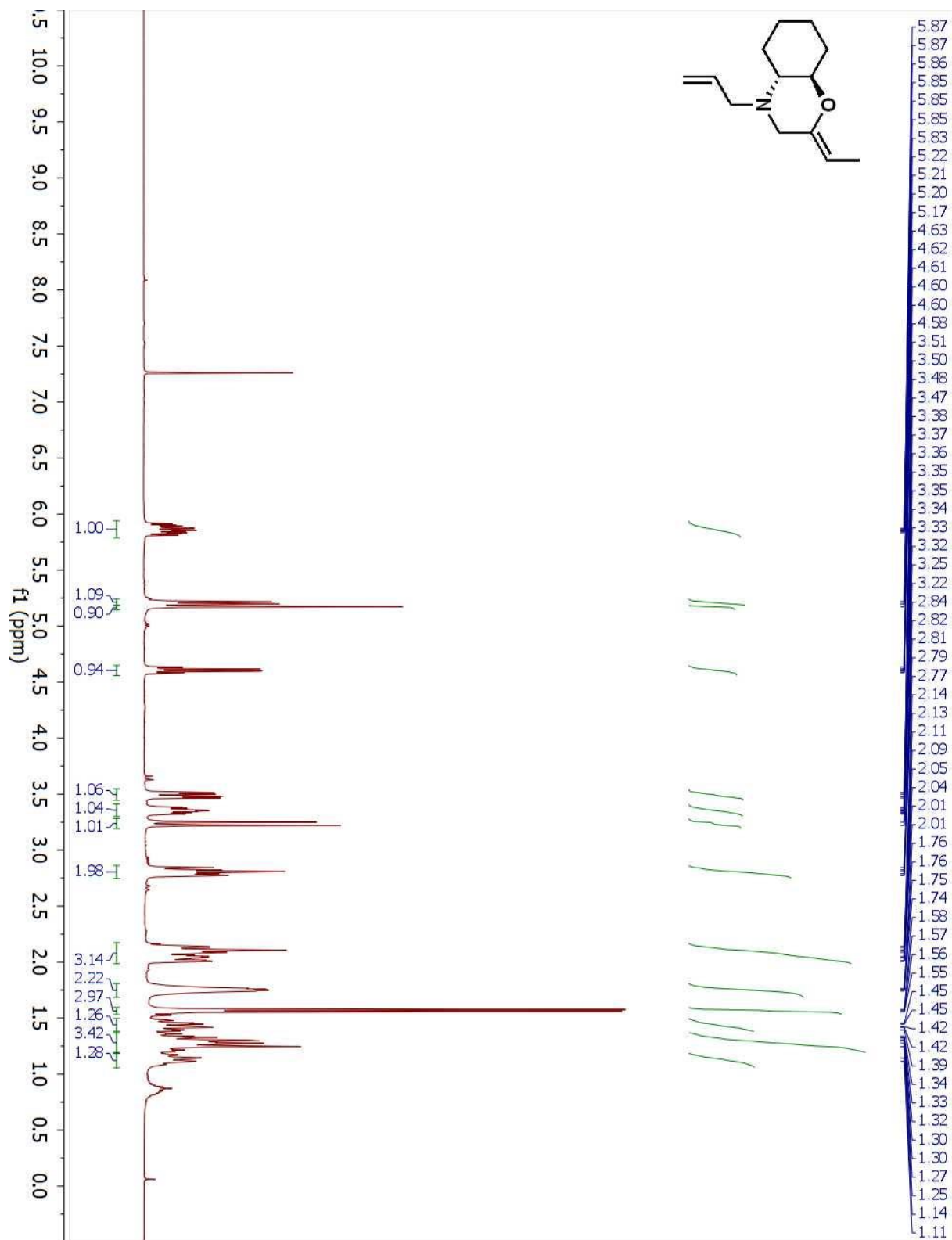


Figure S34. ¹H NMR spectrum of **2d** in CDCl₃.

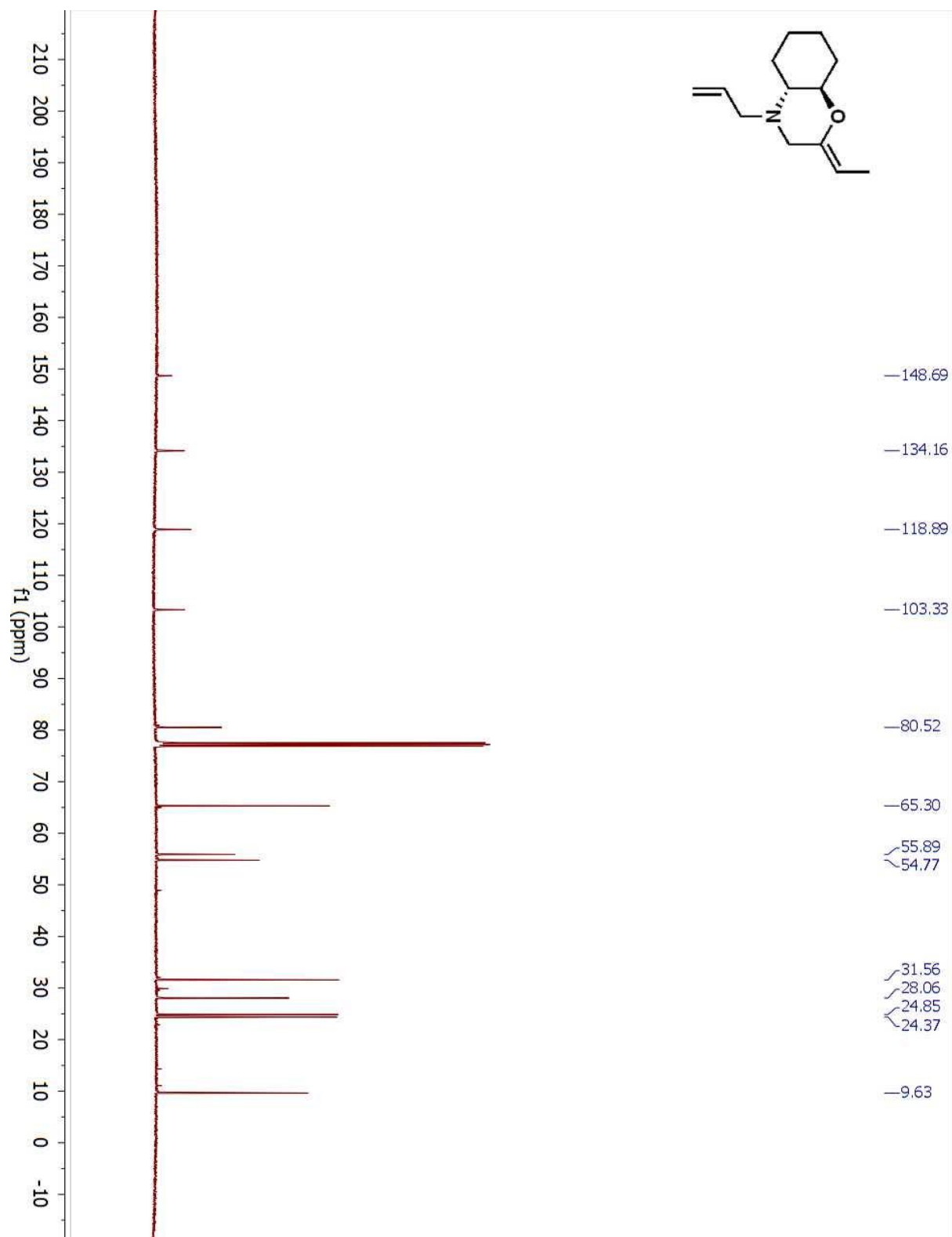
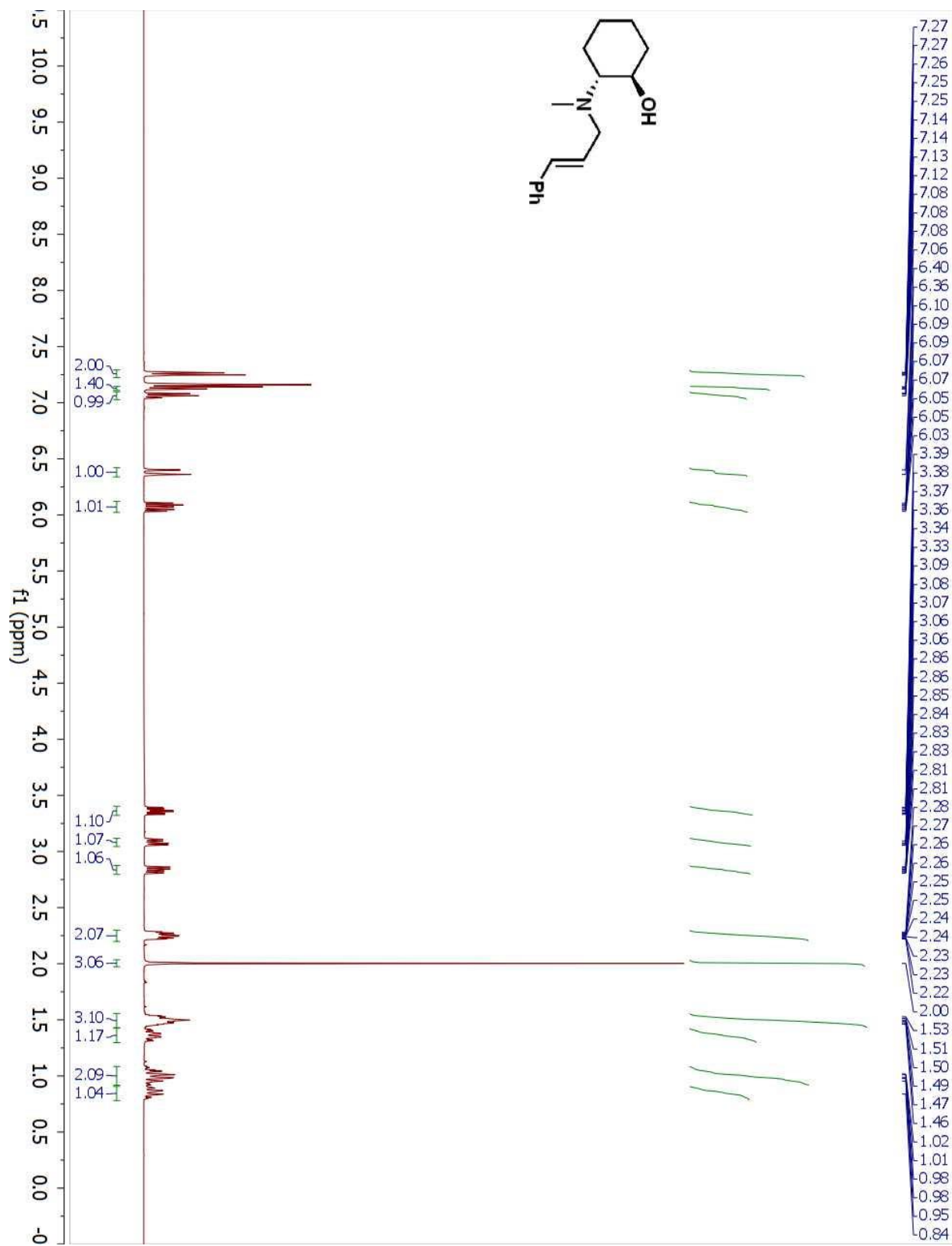


Figure S35. ^{13}C NMR spectrum of **2d** in CDCl_3 .



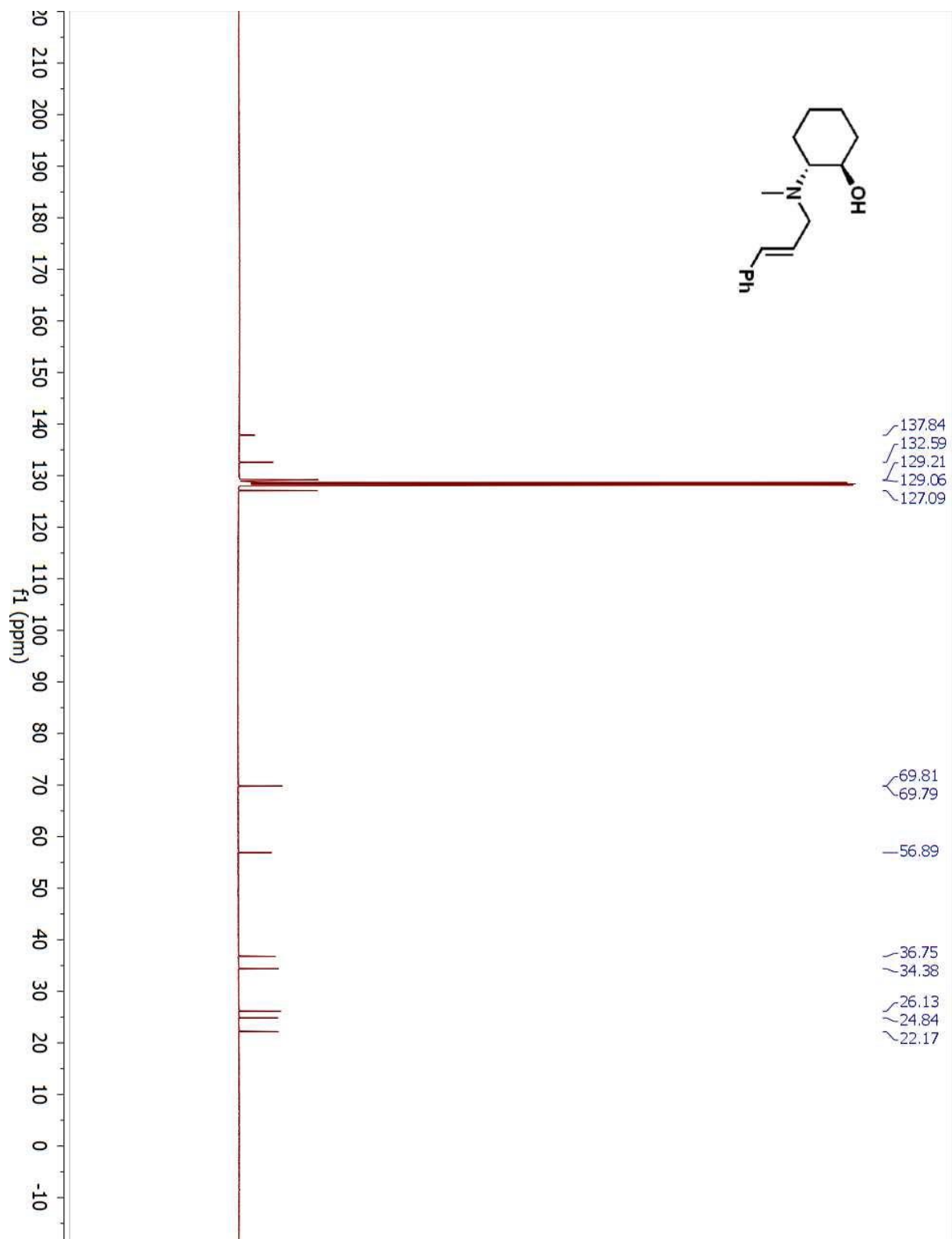


Figure S37. ^{13}C NMR spectrum of **3** in C_6D_6 .

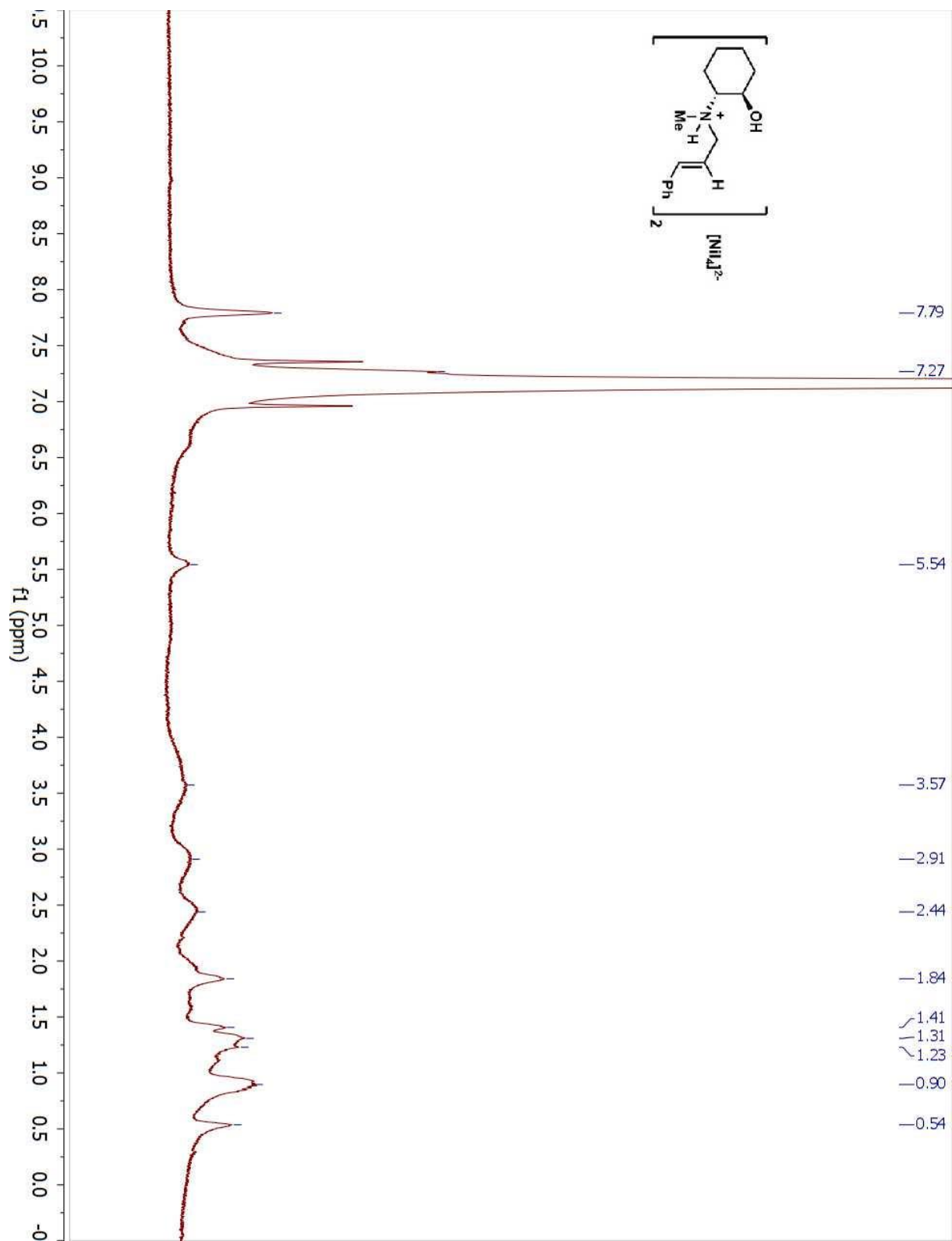


Figure S38. ^1H NMR spectrum of **4** in C_6D_6 .

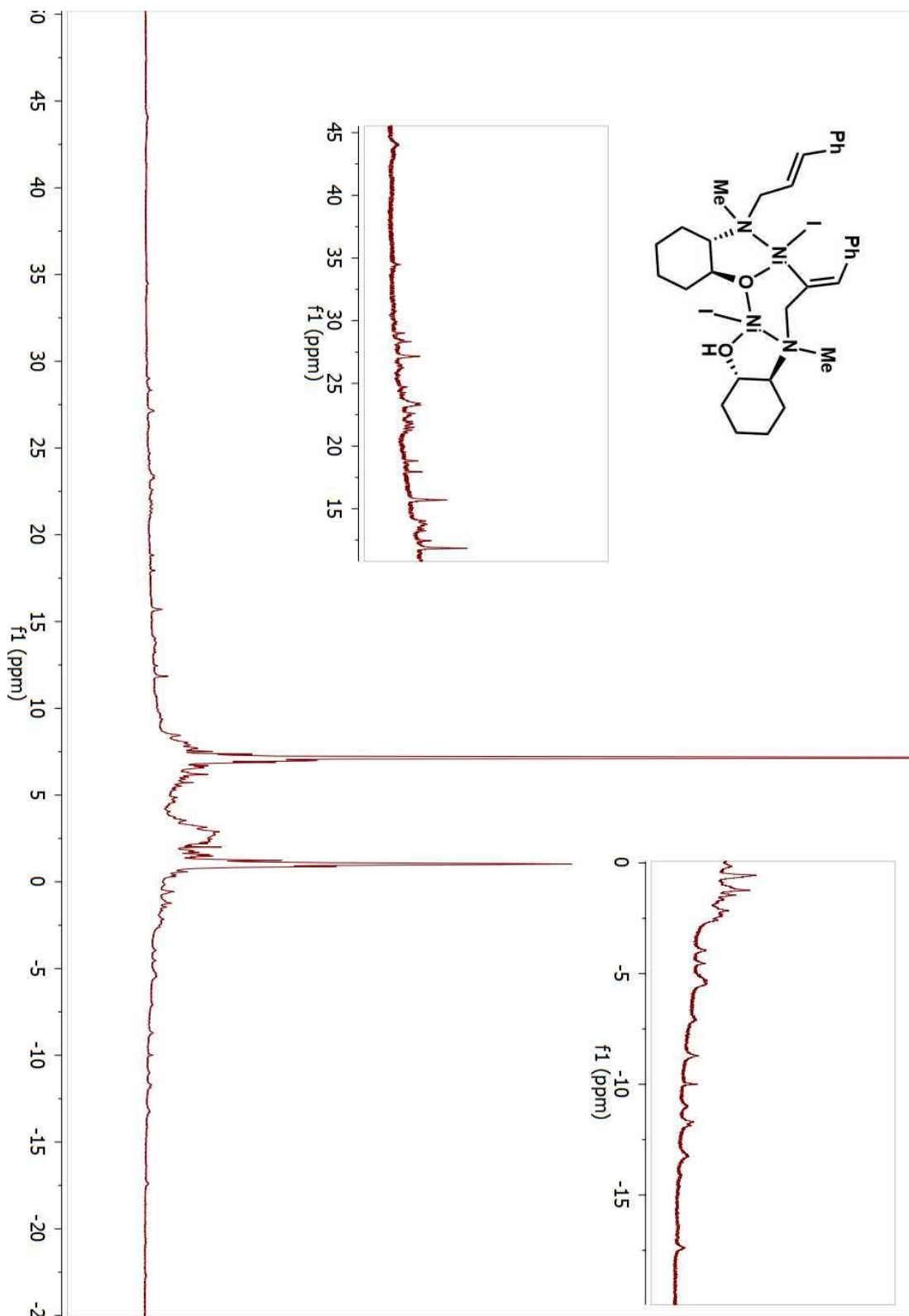


Figure S39. ^1H NMR spectrum of **5** in C_6D_6 .

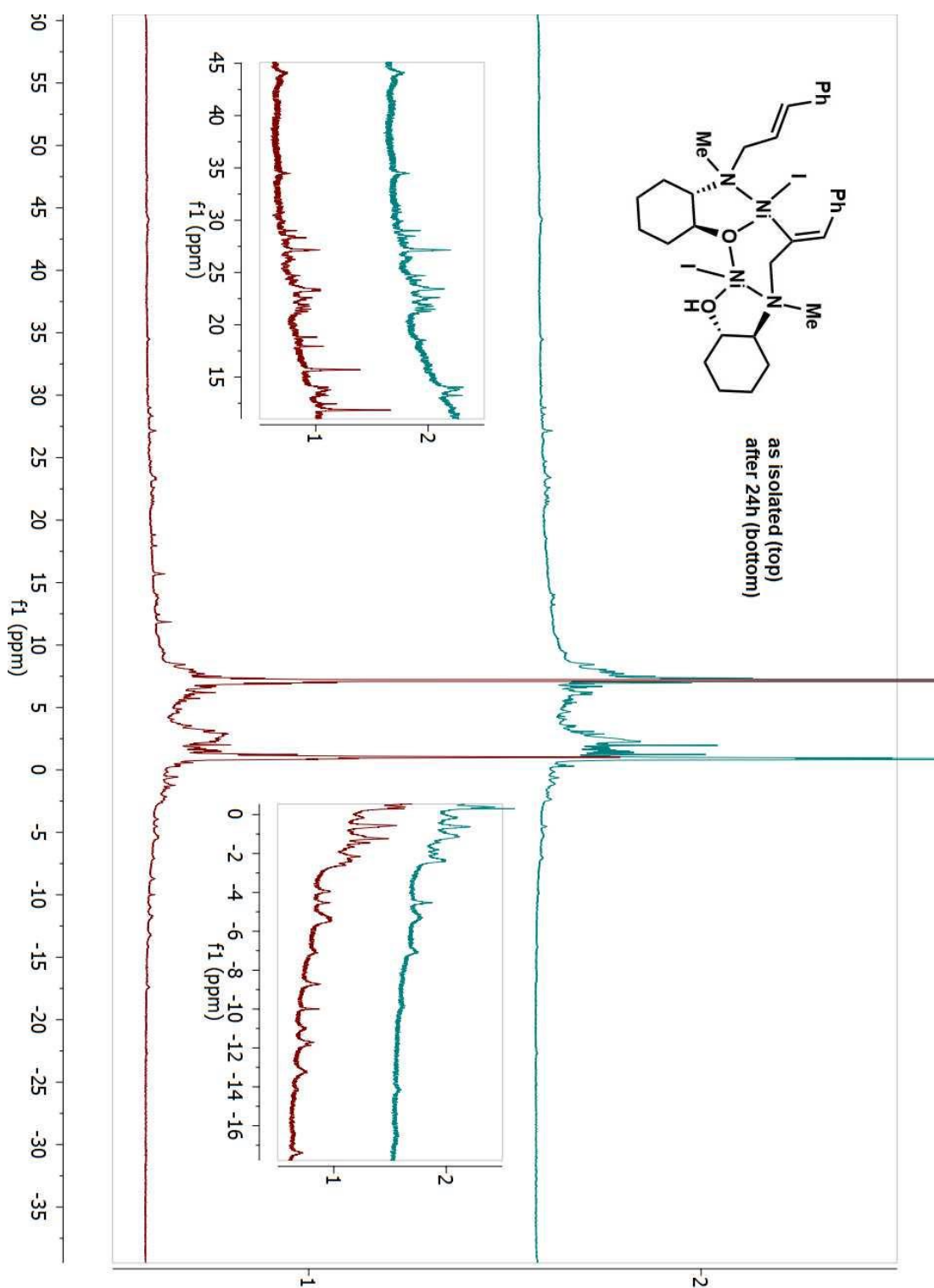


Figure S40. Stacked ^1H NMR spectra of compound **5** (top) and its decomposition products(s) **5'** in C_6D_6 .

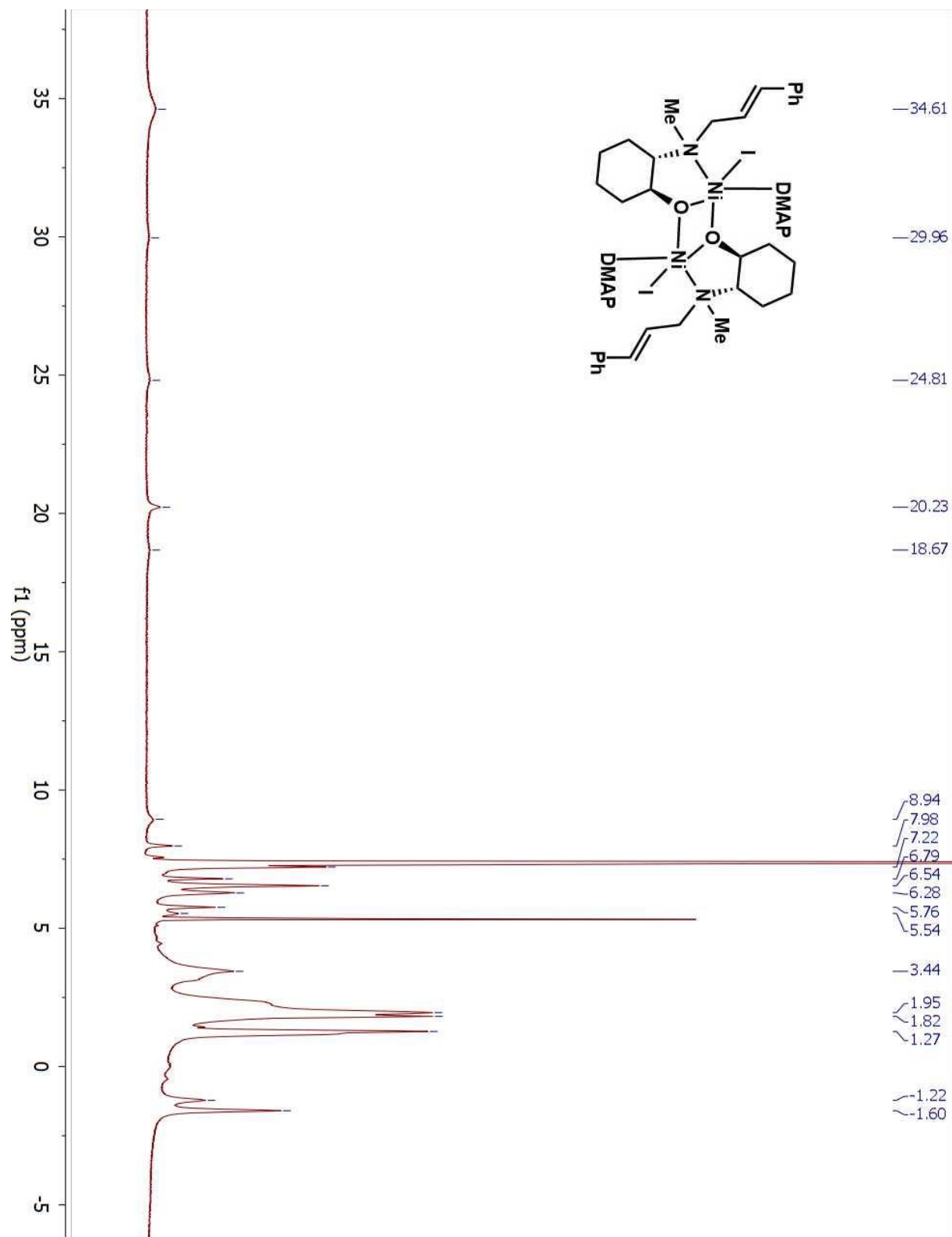


Figure S41. ^1H NMR spectrum of **6** in CD_2Cl_2 .

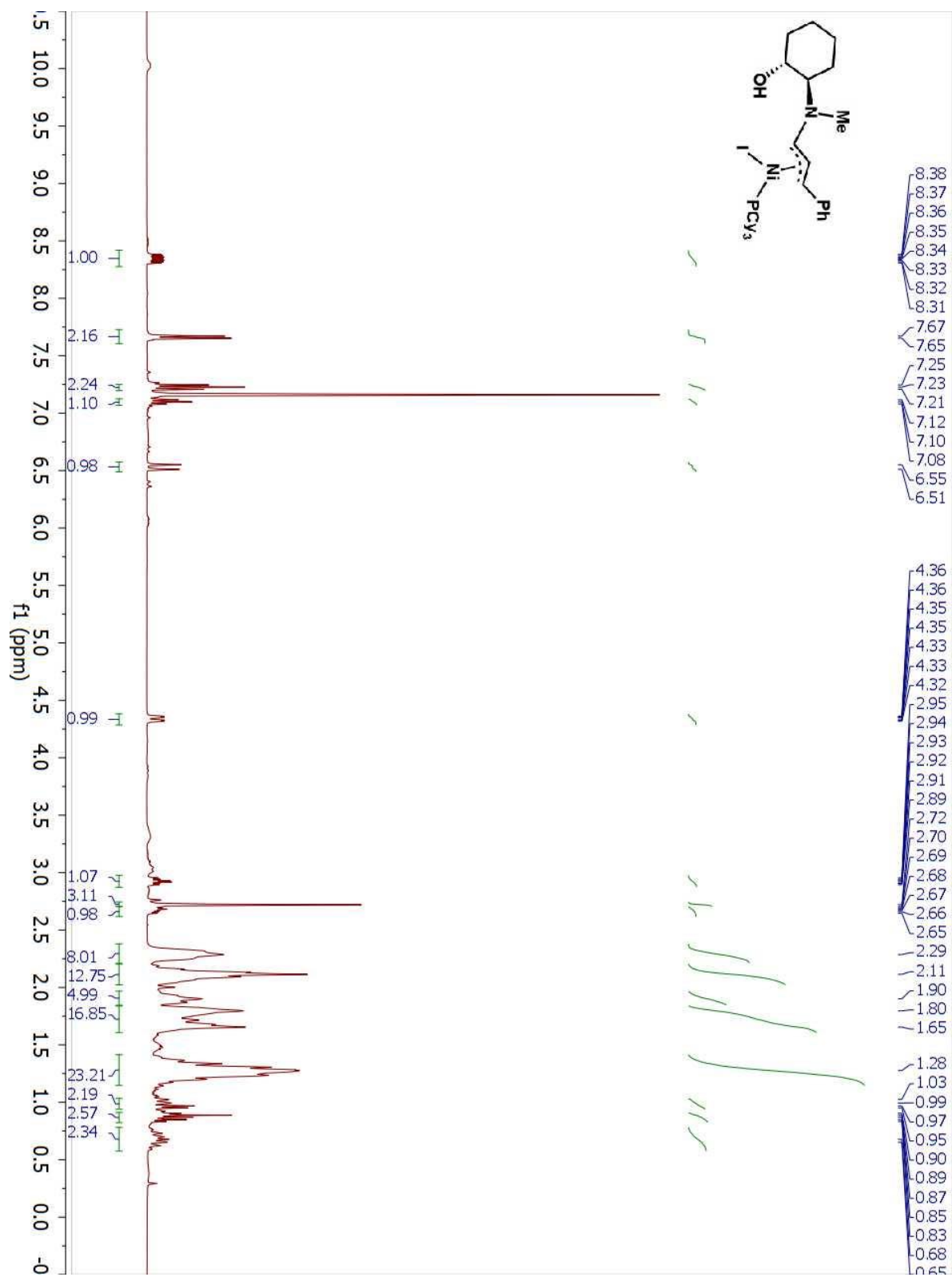


Figure S42. ¹H NMR spectrum of **7** in C₆D₆.

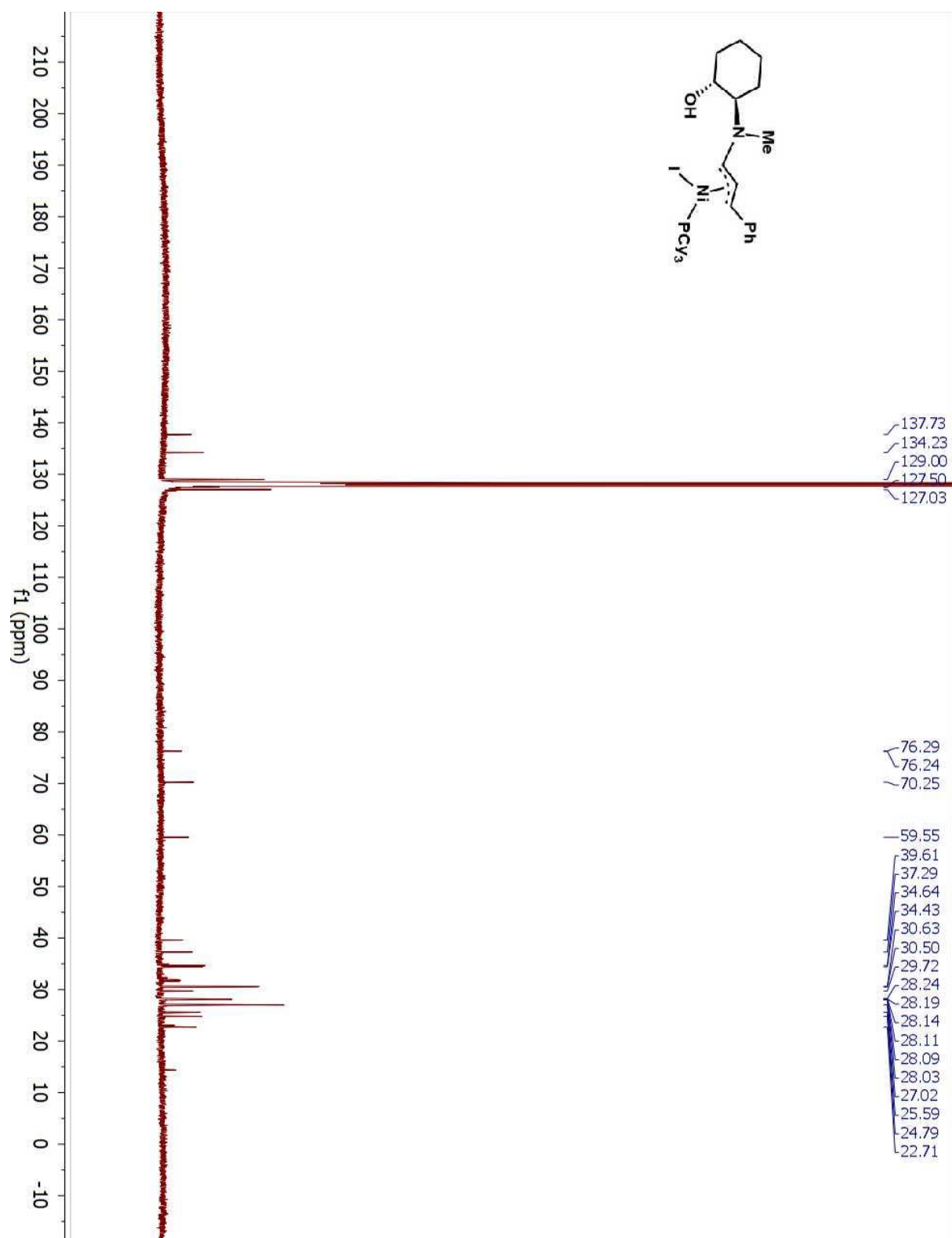


Figure S43. ¹³C NMR spectrum of **7** in C₆D₆.

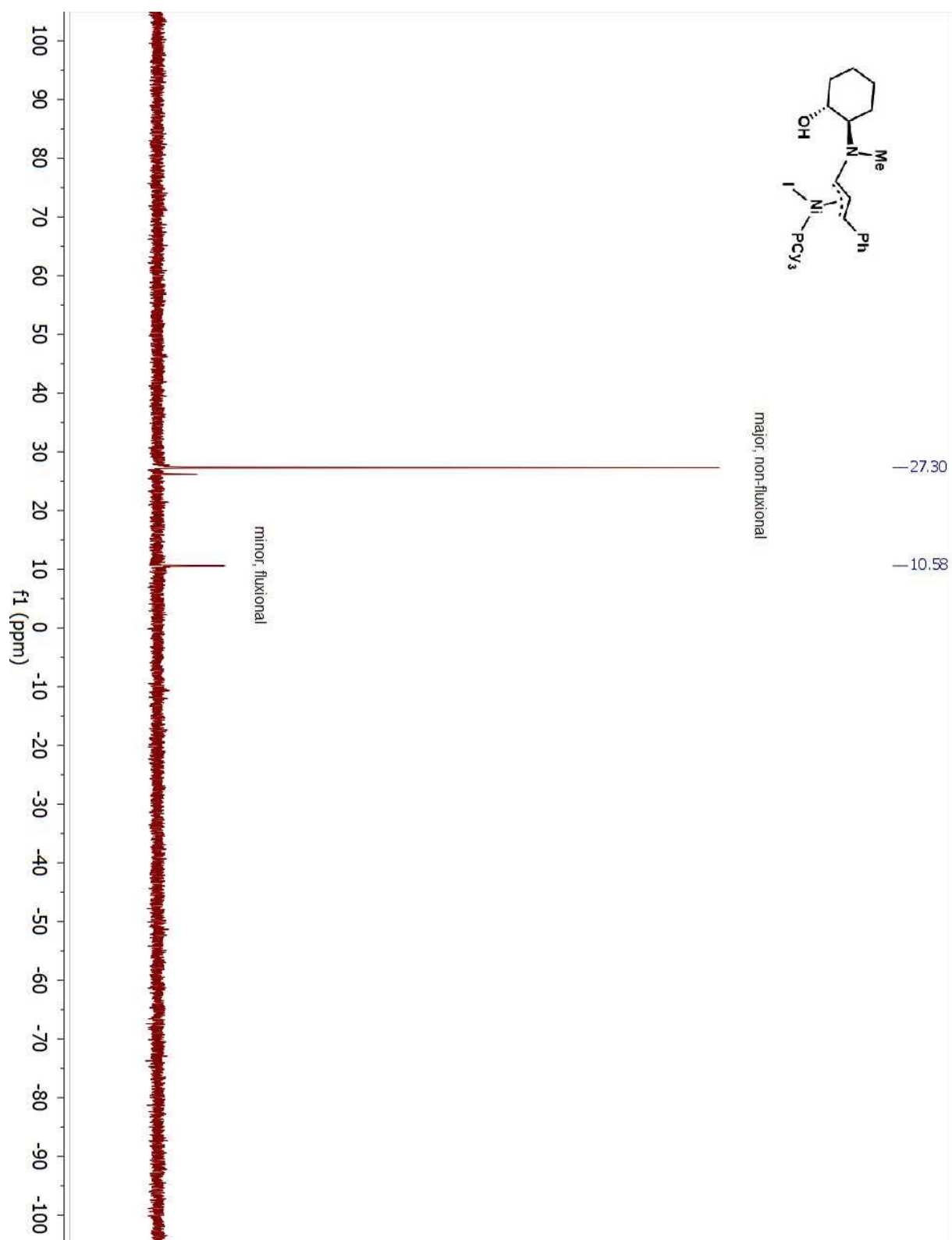


Figure S44. ^{31}P NMR spectrum of compound **7** in C_6D_6 . The small, broadened upfield peak is associated with the minor diastereomer, which displayed broadened resonances in the ^1H NMR spectrum.

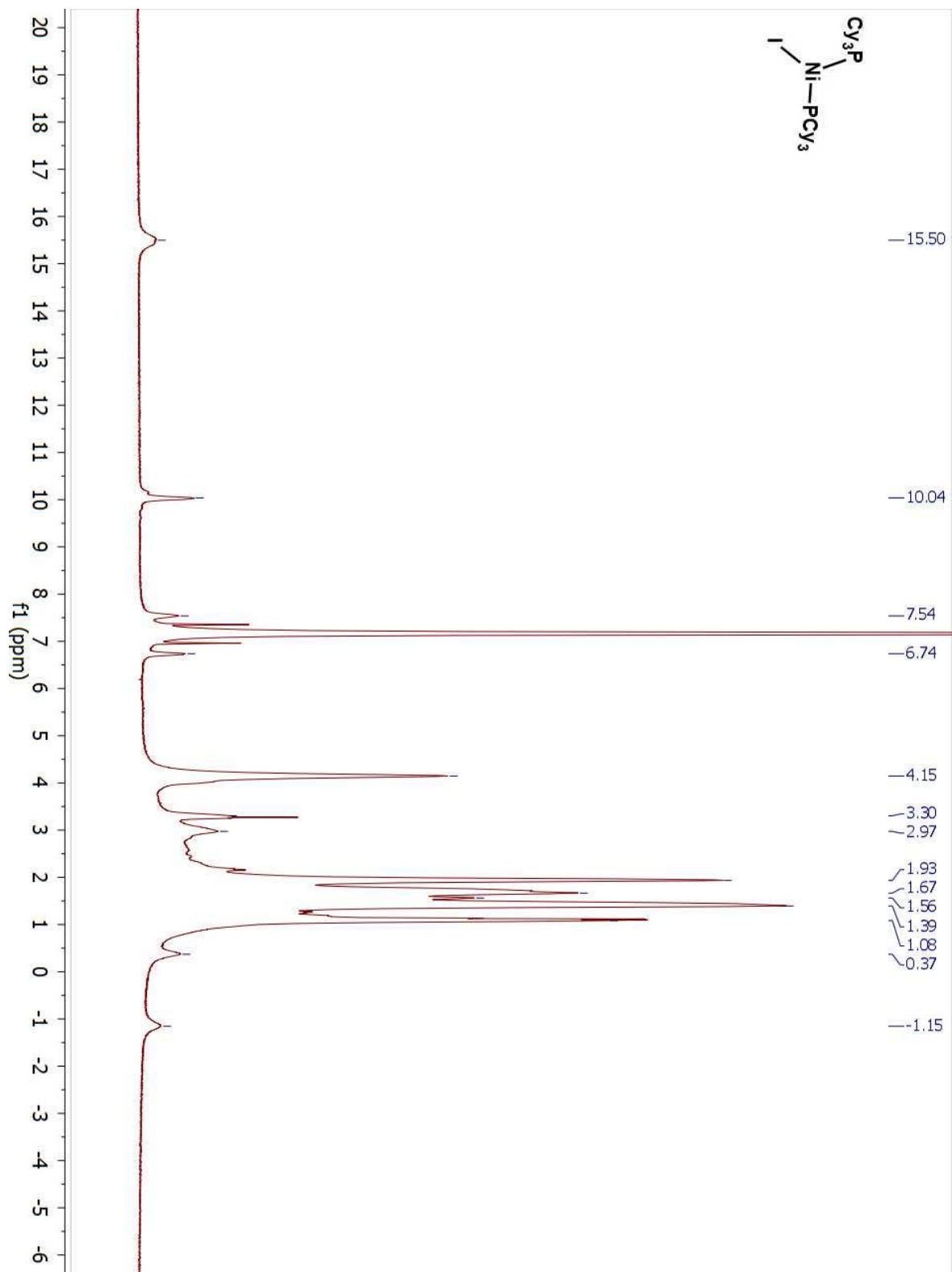


Figure S45. ^1H NMR spectrum of $(\text{PCy}_3)_2\text{NiI}$ in C_6D_6 .

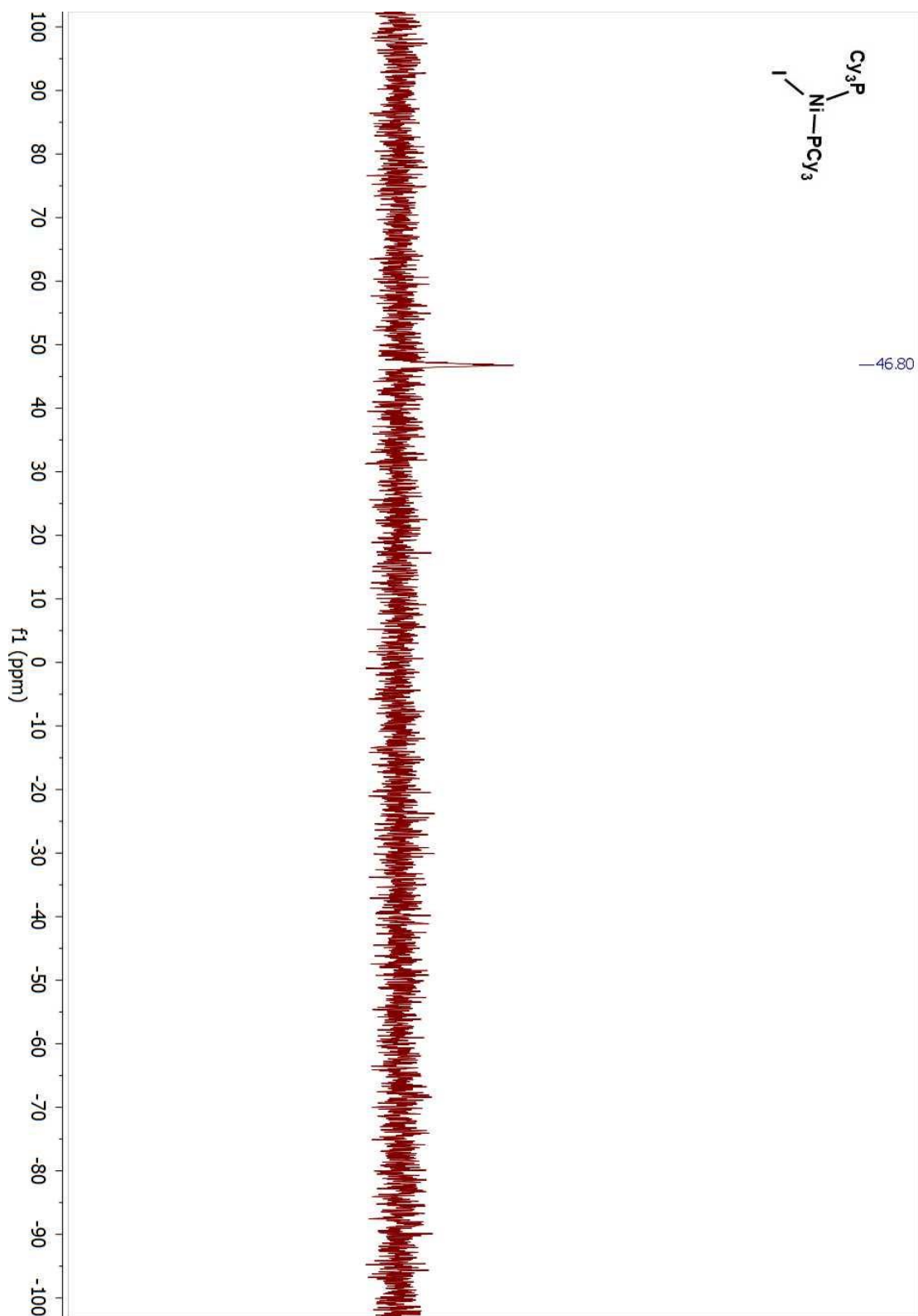


Figure 46. ^{31}P NMR spectrum of $(\text{PCy}_3)_2\text{NiI}$ in C_6D_6 .

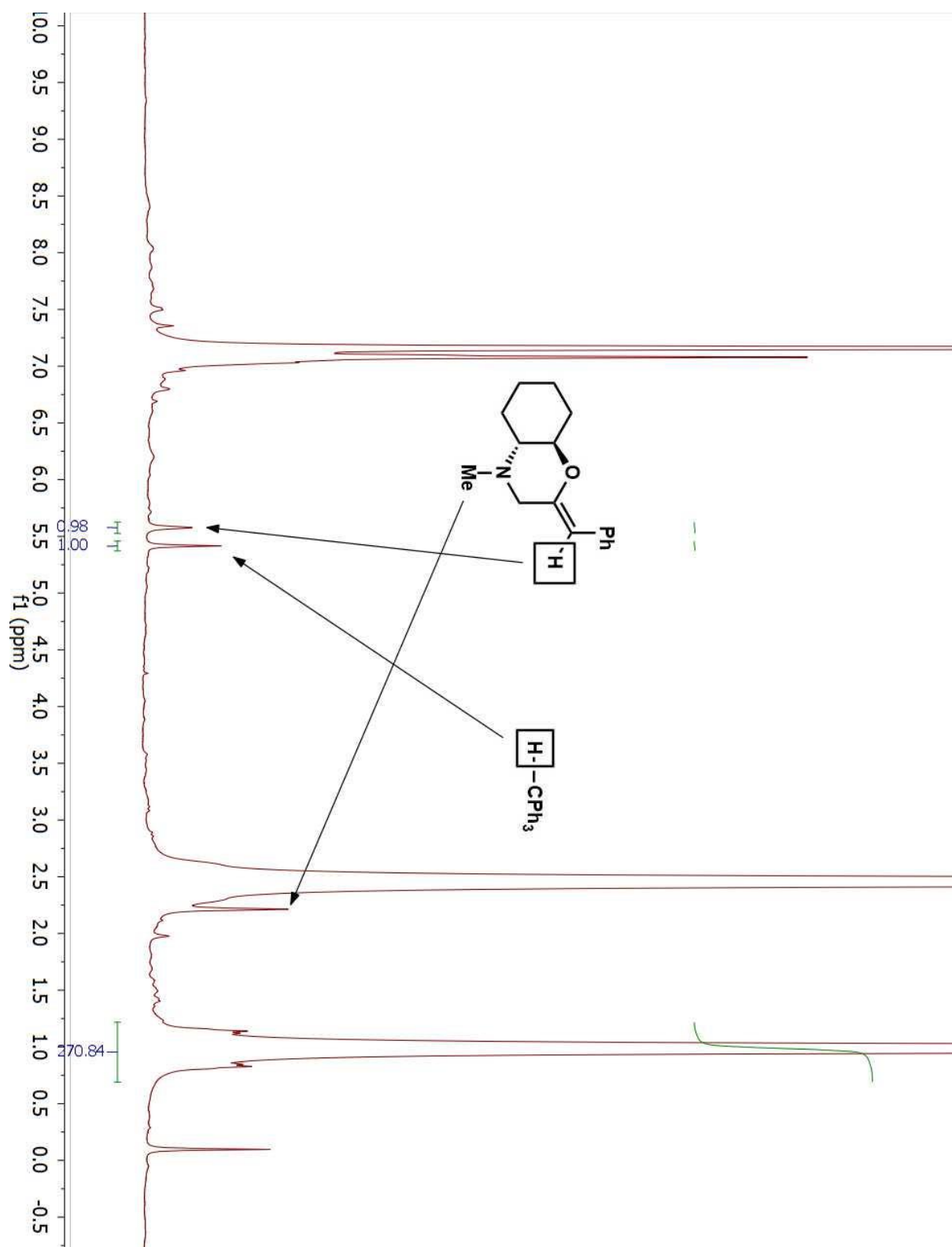


Figure S47. ^1H NMR spectrum of **5** following exposure to ca. 120 equiv of Et_3N in C_6D_6 for 30 minutes at 23 °C. Key resonances assigned to **2f** and a triphenylmethane internal standard are identified with arrows. Quantities: 8.0 mg of **5**, 1.0 mg of HCPH_3 . Equivalents of Et_3N are estimated based on the relative integration of its resonances to that of HCPH_3 .

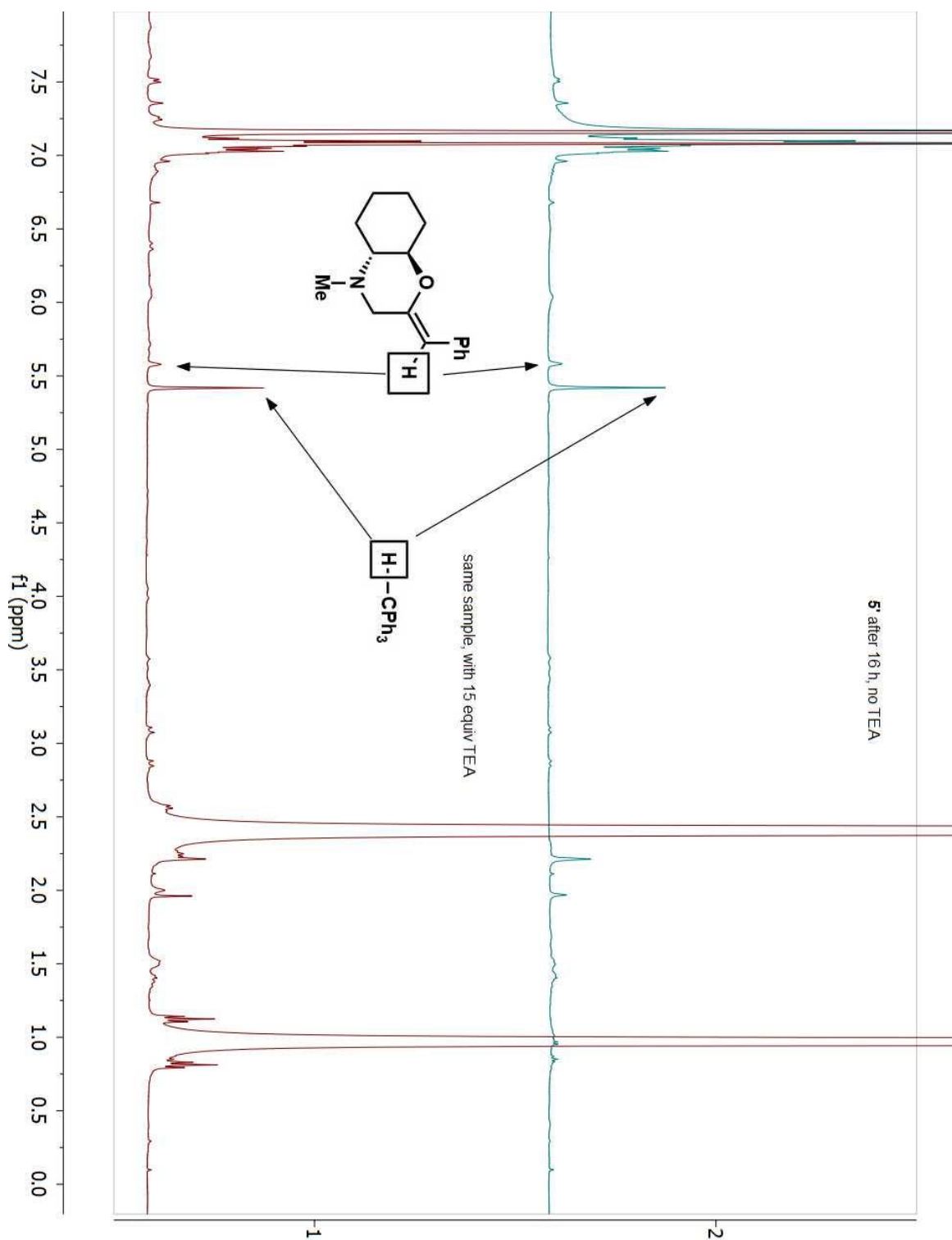


Figure S48. Stacked ^1H NMR spectra of **5'** before and after the addition of ca. 15 equivalents of Et_3N . 5.0 mg of **5** were allowed to decompose at ca. 23 $^\circ\text{C}$ for 16 h with 1.1 mg of a HCPh_3 internal standard. The second spectrum was collected ca. 2 h following the addition of base. The ratio of **2f** to HCPh_3 is ca. 0.22:1.00 in both spectra, indicating a 19% spectroscopic yield.

References

1. Han, S.-J.; Doi, R.; Stoltz, B. M. Nickel-Catalyzed Intramolecular C–O Bond Formation: Synthesis of Cyclic Enol Ethers. *Angew. Chem. Int. Ed.* **2016**, *55*, 7437–7440.
2. Sekar, G.; Singh, V. K. An Efficient Method for Cleavage of Epoxides with Aromatic Amines. *J. Org. Chem.* **1999**, *64*, 287–289.
3. Hoberg, H.; Radine, K.; Krüger, C.; Romão, M. J. Synthesis of New Phosphine Nickel(I) Complexes and Crystal Structure of μ_3 -Iodo-tris-iodo-cyclotris(triphenylphosphine Nickel), (TPP)₃Ni₃I₄. *Z. Naturforsch. B* **1985**, *40b*, 607–614.
4. APEX3, SADABS, and SAINT. Bruker AXS. Madison, WI, USA.
5. Sheldrick, G.M. SHELXT – Integrated space-group and crystal-structure determination. *Acta Cryst.* **2015**, *A71*, 3–8.
6. Sheldrick, G.M. Crystal structure refinement with SHELXL. *Acta Cryst.* **2015**, *C71*, 3–8.
7. Farrugia, L. J. WinGX and ORTEP for Windows: an update. *J. Appl. Cryst.* **2012**, *45*, 849–854.
8. Spek, A. L. PLATON SQUEEZE: a tool for the calculation of the disordered solvent contribution to the calculated structure factors. *Acta Cryst.* **2015**, *C71*, 9–18.
9. Macrae, C. F.; Sovago, I.; Cottrell, S. J.; Galek, P. T. A.; McCabe, P.; Pidcock, E.; Platings, M.; Shields, G. P.; Stevens, J. S.; Towler, M.; Wood, P. A. Mercury 4.0: from visualization to analysis, design and prediction. *J. Appl. Cryst.* **2020**, *53*, 226–235.
10. (a) Neese, F. Software Update: The ORCA Program System, Version 4.0. *Wiley Interdiscip. Rev.: Comput. Mol. Sci.* **2018**, *8*, No. e1327. (b) Neese, F. The ORCA Program System. *Wiley Interdiscip. Rev.: Comput. Mol. Sci.* **2012**, *2*, 73–78.
11. Adamo, C.; Barone, V. Toward Reliable Density Functional Methods without Adjustable Parameters: The PBE0 Model. *J. Chem. Phys.* **1999**, *110*, 6158–6170.
12. (a) Caldeweyher, E.; Ehlert, S.; Hansen, A.; Neugebauer, H.; Spicher, S.; Bannwarth, C.; Grimme, S. A Generally Applicable Atomic-Charge Dependent London Dispersion Correction. *J. Chem. Phys.* **2019**, *150* (15), 154122. (b) Caldeweyher, E.; Bannwarth, C.; Grimme, S. Extension of the D3 Dispersion Coefficient Model. *J. Chem. Phys.* **2017**, *147* (3), 034112.
13. Weigend, F.; Ahlrichs, R. Balanced Basis Sets of Split Valence, Triple Zeta Valence and Quadruple Zeta Valence Quality for H to Rn: Design and Assessment of Accuracy. *Phys. Chem. Chem. Phys.* **2005**, *7* (18), 3297–3305.
14. Peterson, K. A.; Figgen, D.; Goll, E.; Stoll, H.; Dolg, M. Systematically Convergent Basis Sets with Relativistic Pseudopotentials. II. Small-Core Pseudopotentials and Correlation Consistent Basis Sets for the Post-*d* Group 16–18 Elements. *The Journal of Chemical Physics* **2003**, *119* (21), 11113–11123.
15. Barone, V.; Cossi, M. Quantum Calculation of Molecular Energies and Energy Gradients in Solution by a Conductor Solvent Model. *J. Phys. Chem. A* **1998**, *102* (11), 1995–2001.
16. Garcia-Ratés, M.; Neese, F. Effect of the Solute Cavity on the Solvation Energy and Its Derivatives within the Framework of the Gaussian Charge Scheme. *Journal of Computational Chemistry* **2020**, *41* (9), 922–939.
17. Ishida, K.; Morokuma, K.; Komornicki, A. The Intrinsic Reaction Coordinate. An Ab Initio Calculation for HNC→HCN and H→CH₄→CH₄+H⁻. *J. Chem. Phys.* **1977**, *66* (5), 2153–2156.
18. Zhao, Y.; Truhlar, D. G. The M06 Suite of Density Functionals for Main Group Thermochemistry, Thermochemical Kinetics, Noncovalent Interactions, Excited States, and Transition Elements: Two New Functionals and Systematic Testing of Four M06-Class Functionals and 12 Other Functionals. *Theor Chem Account* **2008**, *120* (1), 215–241.
19. Grimme, S. Supramolecular Binding Thermodynamics by Dispersion-Corrected Density Functional Theory. *Chemistry – A European Journal* **2012**, *18* (32), 9955–9964.
20. Izato, Y.; Matsugi, A.; Koshi, M.; Miyake, A. A Simple Heuristic Approach to Estimate the Thermochemistry of Condensed-Phase Molecules Based on the Polarizable Continuum Model. *Phys. Chem. Chem. Phys.* **2019**, *21* (35), 18920–18929.
21. Finkelstein, A. V.; Janin, J. The Price of Lost Freedom: Entropy of Bimolecular Complex Formation. *Protein Engineering, Design and Selection* **1989**, *3* (1), 1–3.
22. Neese, F.; Wennmohs, F.; Hansen, A.; Becker, U. Efficient, Approximate and Parallel Hartree-Fock and Hybrid DFT Calculations. A ‘Chain-of-Spheres’ Algorithm for the Hartree-Fock Exchange. *Chemical Physics* **2009**, *356*, 98–109.
23. Weigend, F. Accurate Coulomb-Fitting Basis Sets for H to Rn. *Phys. Chem. Chem. Phys.* **2006**, *8* (9), 1057–1065.

24. Stoychev, G. L.; Auer, A. A.; Neese, F. Automatic Generation of Auxiliary Basis Sets. *J. Chem. Theory Comput.* **2017**, *13*, 554–562.
25. (a) Ferré, N.; Guihéry, N.; Malrieu, J.-P. Spin Decontamination of Broken-Symmetry Density Functional Theory Calculations: Deeper Insight and New Formulations. *Phys. Chem. Chem. Phys.* **2015**, *17* (22), 14375–14382. (b) Neese, F. Definition of Corresponding Orbitals and the Diradical Character in Broken Symmetry DFT Calculations on Spin Coupled Systems. *Journal of Physics and Chemistry of Solids* **2004**, *65* (4), 781–785.
26. Yamaguchi, K.; Takahara, Y.; Fueno, T. Ab-Initio Molecular Orbital Studies of Structure and Reactivity of Transition Metal-OXO Compounds. In *Applied Quantum Chemistry*; Smith, V. H., Schaefer, H. F., Morokuma, K., Eds.; Springer Netherlands: Dordrecht, 1986; pp 155–184.
27. (a) Schleyer, P. von R.; Maerker, C.; Dransfeld, A.; Jiao, H.; van Eikema Hommes, N. J. R. Nucleus-Independent Chemical Shifts: A Simple and Efficient Aromaticity Probe. *J. Am. Chem. Soc.* **1996**, *118* (26), 6317–6318. (b) Chen, Z.; Wannere, C. S.; Corminboeuf, C.; Puchta, R.; Schleyer, P. von R. Nucleus-Independent Chemical Shifts (NICS) as an Aromaticity Criterion. *Chem. Rev.* **2005**, *105* (10), 3842–3888.
28. (a) Riplinger, C.; Neese, F. An Efficient and near Linear Scaling Pair Natural Orbital Based Local Coupled Cluster Method. *J. Chem. Phys.* **2013**, *138* (3), 034106. (b) Riplinger, C.; Sandhoefer, B.; Hansen, A.; Neese, F. Natural Triple Excitations in Local Coupled Cluster Calculations with Pair Natural Orbitals. *J. Chem. Phys.* **2013**, *139* (13), 134101. (c) Riplinger, C.; Pinski, P.; Becker, U.; Valeev, E. F.; Neese, F. Sparse Maps—A Systematic Infrastructure for Reduced-Scaling Electronic Structure Methods. II. Linear Scaling Domain Based Pair Natural Orbital Coupled Cluster Theory. *J. Chem. Phys.* **2016**, *144* (2), 024109.
29. Bartlett, R. J.; Musiał, M. Coupled-Cluster Theory in Quantum Chemistry. *Rev. Mod. Phys.* **2007**, *79* (1), 291–352.
30. (a) Bertels, L. W.; Lee, J.; Head-Gordon, M. Polishing the Gold Standard: The Role of Orbital Choice in CCSD(T) Vibrational Frequency Prediction. *J. Chem. Theory Comput.* **2021**, *17* (2), 742–755. (b) Fang, Z.; Lee, Z.; Peterson, K. A.; Dixon, D. A. Use of Improved Orbitals for CCSD(T) Calculations for Predicting Heats of Formation of Group IV and Group VI Metal Oxide Monomers and Dimers and UCl₆. *J. Chem. Theory Comput.* **2016**, *12* (8), 3583–3592. (c) Fang, Z.; Vasiliu, M.; Peterson, K. A.; Dixon, D. A. Prediction of Bond Dissociation Energies/Heats of Formation for Diatomic Transition Metal Compounds: CCSD(T) Works. *J. Chem. Theory Comput.* **2017**, *13* (3), 1057–1066.
31. Minenkov, Y.; Wang, H.; Wang, Z.; Sarathy, S. M.; Cavallo, L. Heats of Formation of Medium-Sized Organic Compounds from Contemporary Electronic Structure Methods. *J. Chem. Theory Comput.* **2017**, *13* (8), 3537–3560.
32. T₁ diagnostic defined as the norm of the singles amplitude vector divided by the square root of the number of electrons
33. Stephens, P. J.; Devlin, F. J.; Chabalowski, C. F.; Frisch, M. J. Ab Initio Calculation of Vibrational Absorption and Circular Dichroism Spectra Using Density Functional Force Fields. *J. Phys. Chem.* **1994**, *98* (45), 11623–11627.
34. Mardirossian, N.; Head-Gordon, M. ωB97M-V: A Combinatorially Optimized, Range-Separated Hybrid, Meta-GGA Density Functional with VV10 Nonlocal Correlation. *J. Chem. Phys.* **2016**, *144* (21), 214110.
35. Yu, H. S.; He, X.; Li, S. L.; Truhlar, D. G. MN15: A Kohn–Sham Global-Hybrid Exchange–Correlation Density Functional with Broad Accuracy for Multi-Reference and Single-Reference Systems and Noncovalent Interactions. *Chem. Sci.* **2016**, *7* (8), 5032–5051.
36. For additional examples and discussion see: Funes-Ardoiz, I.; Nelson, D. J.; Maseras, F. Halide Abstraction Competes with Oxidative Addition in the Reactions of Aryl Halides with [Ni(PMe_nPh_(3-n))₄]. *Chem. Eur. J.* **2017**, *23* (66), 16728–16733.
37. Nelsen, S. F.; Blackstock, S. C.; Kim, Y. Estimation of Inner Shell Marcus Terms for Amino Nitrogen Compounds by Molecular Orbital Calculations. *J. Am. Chem. Soc.* **1987**, *109* (3), 677–682.
38. For examples of facile comproportionation from Ni(III) + Ni(I) to 2Ni(II), see (a) Sun, R.; Qin, Y.; Ruccolo, S.; Schnedermann, C.; Costentin, C.; Nocera, D. G. Elucidation of a Redox-Mediated Reaction Cycle for Nickel-Catalyzed Cross Coupling. *J. Am. Chem. Soc.* **2019**, *141* (1), 89–93. (b) Kawamata, Y.; Vantourout, J. C.; Hickey, D. P.; Bai, P.; Chen, L.; Hou, Q.; Qiao, W.; Barman, K.; Edwards, M. A.; Garrido-Castro, A. F.; deGruyter, J. N.; Nakamura, H.; Knouse, K.; Qin, C.; Clay, K. J.; Bao, D.; Li, C.; Starr, J. T.; Garcia-Irizarry, C.; Sach, N.; White, H. S.; Neurock, M.; Minter, S. D.; Baran, P. S. Electrochemically Driven, Ni-Catalyzed Aryl Amination: Scope, Mechanism, and Applications. *J. Am. Chem. Soc.* **2019**, *141* (15), 6392–6402.
39. Knizia, G. Intrinsic Atomic Orbitals: An Unbiased Bridge between Quantum Theory and Chemical Concepts. *J. Chem. Theory Comput.* **2013**, *9* (11), 4834–4843.